



# Simulating transient wave phenomena in acoustic metamaterials using auxiliary fields

Cédric Bellis, Bruno Lombard

## ► To cite this version:

Cédric Bellis, Bruno Lombard. Simulating transient wave phenomena in acoustic metamaterials using auxiliary fields. Wave Motion, 2019, 86, pp.175-194. hal-02004847

**HAL Id: hal-02004847**

**<https://hal.science/hal-02004847>**

Submitted on 2 Feb 2019

**HAL** is a multi-disciplinary open access archive for the deposit and dissemination of scientific research documents, whether they are published or not. The documents may come from teaching and research institutions in France or abroad, or from public or private research centers.

L'archive ouverte pluridisciplinaire **HAL**, est destinée au dépôt et à la diffusion de documents scientifiques de niveau recherche, publiés ou non, émanant des établissements d'enseignement et de recherche français ou étrangers, des laboratoires publics ou privés.

# Simulating transient wave phenomena in acoustic metamaterials using auxiliary fields

C. Bellis<sup>a</sup>, B. Lombard<sup>a,\*</sup>

<sup>a</sup>*Aix Marseille Univ, CNRS, Centrale Marseille, LMA, Marseille, France*

---

## Abstract

Acoustic wave propagation in dispersive metamaterials is considered. A prototypical example stems from the homogenization of a waveguide coupled with Helmholtz resonators and elastic membranes. The homogenized models of acoustic metamaterials are characterized by constitutive parameters, namely the effective bulk modulus and the effective mass density, that are frequency dependent. In this context, the objective considered here is to analyze such media in the time-domain and to simulate associated transient wave phenomena. To do so, the governing evolution equations are recast using a set of auxiliary fields to obtain an augmented first-order hyperbolic system. This initial-value problem is analyzed and then solved numerically using a splitting method and a high-order finite-difference scheme. An immersed interface method is also implemented to tackle scattering and interface problems involving metamaterial subdomains of arbitrary shapes. Numerical experiments are performed to validate the proposed overall approach and to investigate a variety of transient wave phenomena occurring in acoustic metamaterials.

*Keywords:* negative index materials, band-gap, perfect lensing, augmented hyperbolic systems, scientific computing

---

## Highlights

- Wave phenomena arising in dispersive acoustic metamaterials are considered.
- This problem is addressed based on an augmented time-domain formulation with auxiliary fields.
- The augmented system is shown to be mathematically well-posed with smooth solutions.
- These solutions are computed numerically using schemes that are standard for nondispersive media.
- The proposed implementation is validated using semianalytical solutions.
- Examples are discussed to highlight the flexibility and efficiency of the proposed approach.

## 1. Introduction

Metamaterials are man-made structures designed to manipulate the propagation of waves in ways that does not occur in natural media [10, 11]. They involve frequency-dependent effective parameters that are negative on some frequency ranges, which yields a Poynting vector in opposite direction with the wave vector. It opens the door to exotic behaviors (e.g. negative refraction) and new applications: ultra-thin acoustic barriers, acoustical lenses whose resolution surpasses the diffraction limit, acoustical cloaking, to cite a few [20, 33, 21]. The first and most-widely known acoustic metamaterial (AMM), designed to isolate low-frequency waves much more efficiently than the classical mass law, was proposed by Liu and co-authors [29]. It relies on a composite medium containing microstructural elements with heavy masses surrounded by a soft rubber annulus arranged periodically in a 3D solid matrix. The concept of double-negative acoustic medium, involving both negative densities and bulk modulus, paves the way to perfect lenses [38]. It has been

---

\*Corresponding author

Email addresses: bellis@lma.cnrs-mrs.fr (C. Bellis), lombard@lma.cnrs-mrs.fr (B. Lombard)

theoretically investigated by various authors in composite media involving different resonant mechanisms [26, 12].

In 2006, Fang and his collaborators [14] found experimentally a negative effective bulk modulus near the resonant frequency in a structured medium consisting of a 1D array of subwavelength Helmholtz resonators (HRs). The design of such medium has significantly broadened the design variety of locally-resonant acoustic materials [9]. Based on tensioned thin membranes, negative density has been predicted theoretically in 2008 by Yang and his collaborators [47], and then obtained experimentally in 2009 by Lee and coauthors [23]. Combining HRs with elastic membranes has enabled to build double negative AMM [44]. The four different combinations of effective density and elastic modulus can then be achieved by a judicious design of the resonance frequencies. From a theoretical standpoint, a generalization of Newton's second law and continuum elastodynamics has been proposed by Milton and Willis in 2007 to describe the effective behavior of composite media [35]. This framework provides a physical interpretation for the effective density and bulk modulus that characterize AMM, see also [24].

The governing equations in resonant AMM are originally formulated in the frequency domain, which has motivated the development of dedicated numerical approaches such as the transmission line method [9]. To tackle broadband acoustic experiments it is advantageous to consider time-domain formulations. To this end, a set of auxiliary fields can be introduced as it has been done in a number of studies on Maxwell's equations, see [45, 18, 19, 6, 7]. Based on this formalism, various methods have been proposed in the transient regime for computational electromagnetism, based on the finite-element method [27], the discontinuous Galerkin method [28] and the staggered-grid finite-difference method [46]. Moreover, for Maxwell's equations in dispersive metamaterials, mathematical properties such as well-posedness have been recently investigated in [37].

In this context, our overarching goal is to investigate the broad spectrum of transient wave phenomena that can arise in acoustic metamaterials, such as propagation regimes in double-negative materials, as well as wave scattering or interface problems. To do so, our objective is twofold:

- (i) Demonstrate that, by using auxiliary fields, the governing evolution equations can be recast as an augmented system that is well-posed and has smooth solutions in the time-domain. Well-posedness is proven by a direct application of Friedrichs' theory on symmetric hyperbolic systems [17] rather than using the classic Hille-Yoshida theory of semi-groups [6].
- (ii) Show that this system can be solved numerically using methods that are standard for nondispersive media, thus providing a practical and efficient approach to study transient phenomena in dispersive acoustic metamaterials.

Some prototypical and frequency-dependent constitutive laws are considered in this article for the effective density and bulk modulus. For such models we investigate an equivalent time-domain formulation that employs a set of auxiliary fields. It should be noted that the mathematical analysis of the existence of a limit absorption principle [42] for the configurations considered is beyond the scope of this study. The obtained augmented first-order hyperbolic system and its solutions in free-space are analyzed. Then, we propose a novel time-domain numerical approach based on a splitting method and a high-order finite-difference ADER scheme. The proposed time-marching scheme is characterized by an optimal numerical stability condition that is independent of the dissipation and dispersion effects. Moreover, an immersed interface method is introduced to tackle interface problems and scattering by metamaterials. This method allows in particular to discretize arbitrary-shaped interfaces while preventing from the classical drawbacks of Cartesian grid methods (spurious diffractions, loss of convergence order); see [32] and references therein. For the sake of clarity, most developments are illustrated numerically in a 1D configuration which is representative of a waveguide coupled with HRs and elastic membranes but a number of 2D numerical experiments are also discussed.

The article outline is as follows. In Section 2, the physical model of interest is described and the corresponding time-domain formulation is established with the introduction of auxiliary fields. The key properties of the obtained augmented system and of its solutions are provided in Section 3. Section 4 focuses on the numerical modeling and these overall developments are illustrated in Section 5 in a 1D configuration for which the simulations are validated by comparison with semianalytical solutions. A set of 2D numerical experiments is also presented, with less details, to illustrate the applicability of our approach

to more challenging configurations.

## 2. Acoustic metamaterial modeling

### 2.1. Effective parameters

Consider the classical time-domain equations of acoustics in a homogeneous medium which, given some source terms  $\mathbf{g}$  and  $h$ , govern the evolution of the acoustic velocity and pressure fields  $\mathbf{v}$  and  $p$  respectively for  $\mathbf{x} \in \mathbb{R}^d$  and  $t > 0$ :

$$\begin{cases} \rho_a \frac{\partial \mathbf{v}}{\partial t}(\mathbf{x}, t) + \nabla p(\mathbf{x}, t) = \rho_a \mathbf{g}(\mathbf{x}, t), \\ \kappa_a^{-1} \frac{\partial p}{\partial t}(\mathbf{x}, t) + \operatorname{div} \mathbf{v}(\mathbf{x}, t) = \kappa_a^{-1} h(\mathbf{x}, t). \end{cases} \quad (1)$$

The parameters  $\rho_a > 0$  and  $\kappa_a > 0$  denote the mass density and bulk modulus respectively. Accordingly, one defines  $c_a = \sqrt{\kappa_a / \rho_a}$  as the sound velocity. With the Fourier transform in time of a function  $h(t)$  being denoted as  $\hat{h}(\omega)$ , in terms of the angular frequency  $\omega$ , then (1) is transformed in the Fourier domain as

$$\begin{cases} i\omega \rho_a \hat{\mathbf{v}}(\mathbf{x}, \omega) + \nabla \hat{p}(\mathbf{x}, \omega) = \rho_a \hat{\mathbf{g}}(\mathbf{x}, \omega), \\ i\omega \kappa_a^{-1} \hat{p}(\mathbf{x}, \omega) + \operatorname{div} \hat{\mathbf{v}}(\mathbf{x}, \omega) = \kappa_a^{-1} \hat{h}(\mathbf{x}, \omega). \end{cases} \quad (2)$$

Acoustic metamaterial modeling allows to replace the constitutive parameters  $\rho_a$  and  $\kappa_a^{-1}$  at the left-hand sides of (2) by some frequency-dependent material laws, see [26, 44, 24, 20]. Here we consider the following prototypical mappings:

$$\rho_a \longleftarrow \hat{\rho}(\omega) = \rho_a \left( 1 - \frac{\Omega_\rho^2}{\omega^2 - \omega_\rho^2} \right), \quad (3a)$$

$$\kappa_a^{-1} \longleftarrow \hat{\kappa}^{-1}(\omega) = \kappa_a^{-1} \left( 1 - \frac{\Omega_\kappa^2}{\omega^2 - \omega_\kappa^2 - i\gamma\omega} \right). \quad (3b)$$

The parameter  $\gamma \geq 0$  is a dissipation coefficient that accounts for physical losses, while  $\omega_\rho$  and  $\omega_\kappa$  denote resonance frequencies. The limit-case  $\Omega_\rho = \Omega_\kappa = 0$  in (3) yields  $\hat{\rho} = \rho_a$  and  $\hat{\kappa}^{-1} = \kappa_a^{-1}$ , which coincides with the classical acoustic properties. The parameters  $\hat{\rho}(\omega)$  and  $\hat{\kappa}^{-1}(\omega)$  have to be interpreted as effective material properties that derive from the homogenization of a microstructured medium (an example of physical configuration is discussed in Section 5), to which the positive coefficients  $\Omega_\rho$ ,  $\Omega_\kappa$ ,  $\omega_\rho$ ,  $\omega_\kappa$  and  $\gamma$  can be related. While our objective is neither to discuss the derivation of effective constitutive properties such as (3a) and (3b) nor their particular forms, references can be made to, e.g., [1, 15] for the homogenization of resonant microstructures that lead to effective coefficients such as (3). In this context, the coefficients entering (3), such as  $\Omega_\rho$  and  $\omega_\rho$ , follow from the resolution of cell problems at the scale of the microstructure. The mathematical homogenization process reveals typically an infinite number of resonances but, in practice, it is sufficient to take into account only a finite number of them to tackle wave propagation problems. Therefore and for the sake of clarity, a single resonant term is considered at first in (3a) and (3b) while a generalization to a finite number of resonances is discussed in Section 2.3.

The insertion of the resonant parameters (3) into the equations (2) leads to a set of elliptic equations which, to be solved, requires the formation and inversion of a (possibly large) linear system at each frequency. In the frequency-domain, therefore, performing simulations involving broadband frequency signals can be costly numerically, unlike in a time-domain formulation where such signals can be processed in a single simulation. In this context, we focus on performing time-domain simulations of wave propagation phenomena in resonant acoustic metamaterials. In other words, we address here the generic integration of frequency-dependent laws such as (3) into a time-domain numerical scheme.

## 2.2. Time-domain formulation

### 2.2.1. Auxiliary fields

In acoustic metamaterials, the effective physical parameters  $\rho$  and  $\kappa^{-1}$  entering the governing equations (1) intervene through time-domain convolution operators. The numerical implementation of such nonlocal operators would require storing the entire history of the fields, which is very consuming from a memory point of view and thus prevents from tackling realistic problems in 2D and 3D. Therefore, to perform time-domain simulations, the introduction of auxiliary fields can be used advantageously to obtain a set of evolution equations in a local form. First, one defines the auxiliary field  $\hat{\mathbf{w}}$  by the equation:

$$(\omega^2 - \omega_\rho^2)\hat{\mathbf{w}} = -\hat{\mathbf{v}}.$$

Doing so and given the form of the effective density (3a), this entails:

$$\hat{\rho}(\omega) \hat{\mathbf{v}} = \rho_a \hat{\mathbf{v}} + \rho_a \Omega_\rho^2 \hat{\mathbf{w}}.$$

Likewise, one defines the field  $\hat{r}$  through

$$(\omega^2 - \omega_\kappa^2 - i\gamma\omega)\hat{r} = -\hat{p},$$

so that, from the bulk modulus identity (3b), one obtains for all  $\omega \in \mathbb{R}_+$ :

$$\hat{\kappa}^{-1}(\omega) \hat{p} = \kappa_a^{-1} \hat{p} + \kappa_a^{-1} \Omega_\kappa^2 \hat{r}.$$

Combining the previous identities with the governing equations (2) and applying the inverse Fourier transform in time yields

$$\begin{cases} \frac{\partial \mathbf{v}}{\partial t} + \Omega_\rho^2 \frac{\partial \mathbf{w}}{\partial t} + \frac{1}{\rho_a} \nabla p = \mathbf{g}, \\ \frac{\partial^2 \mathbf{w}}{\partial t^2} + \omega_\rho^2 \mathbf{w} = \mathbf{v}, \\ \frac{\partial p}{\partial t} + \Omega_\kappa^2 \frac{\partial r}{\partial t} + \kappa_a \operatorname{div} \mathbf{v} = h, \\ \frac{\partial^2 r}{\partial t^2} + \gamma \frac{\partial r}{\partial t} + \omega_\kappa^2 r = p. \end{cases}$$

To deal with a first-order system in time, one introduces the additional auxiliary fields  $\mathbf{u}$  and  $q$  such that  $\frac{\partial \mathbf{w}}{\partial t} = \mathbf{u}$  and  $\frac{\partial r}{\partial t} = q$ . Finally, one obtains the following augmented system of evolution equations for all  $\mathbf{x} \in \mathbb{R}^d$  and time  $t > 0$ :

$$\begin{cases} \frac{\partial \mathbf{v}}{\partial t} + \frac{1}{\rho_a} \nabla p + \Omega_\rho^2 \mathbf{u} = \mathbf{g}, \\ \frac{\partial p}{\partial t} + \kappa_a \operatorname{div} \mathbf{v} + \Omega_\kappa^2 q = h, \\ \frac{\partial \mathbf{u}}{\partial t} - \mathbf{v} + \omega_\rho^2 \mathbf{w} = \mathbf{0}, \\ \frac{\partial \mathbf{w}}{\partial t} - \mathbf{u} = \mathbf{0}, \\ \frac{\partial q}{\partial t} - p + \gamma q + \omega_\kappa^2 r = 0, \\ \frac{\partial r}{\partial t} - q = 0. \end{cases} \quad (4)$$

The ensuing analysis aims at showing that the solution  $(\mathbf{v}, p, \mathbf{u}, \mathbf{w}, q, r)$  to the augmented system (4) is unique and smooth, in a  $L^2$  sense. It should be noted that this study does not address the question of the existence of a limiting absorption principle, see [42], for acoustic dispersive media, which is beyond its

scope and not essential for the results given hereafter. This question requires an in-depth analysis as it has been shown in [6] for electromagnetic dispersive media that some nonstandard resonance phenomena arise and therefore they must be expected in acoustic dispersive media too. At these frequencies, the limiting absorption principle fails or holds only on a subspace of source terms that needs to be characterized. The question of the existence of a limiting absorption principle has been also studied in the context of an interface problem involving a dispersive electromagnetic media in [5, 7].

### 2.2.2. Augmented first-order hyperbolic system

It is emphasized that no approximation has been made to transform (2) with the frequency-dependent parameters (3) into the time-domain formulation (4). Nonetheless, this first-order formulation is at the price of handling the auxiliary fields  $\mathbf{u}$ ,  $\mathbf{w}$ ,  $q$  and  $r$  instead of the two original unknowns  $\mathbf{v}$  and  $p$  only. This represents  $m = 3(d + 1)$  fields overall instead of  $d + 1$ , which increases the memory requirements. However, the additional fields satisfy some linear ODEs (instead of PDEs), which results in an additional CPU cost largely smaller than a factor 3. Typically, going from (1) to (4) implies, in our implementation, an extra cost in computation time of a factor 0.3 in 1D.

Accordingly, one introduces the vector of unknown  $\mathbf{U} : \mathbb{R}^d \times [0, +\infty[ \rightarrow \mathbb{R}^m$  as

$$\mathbf{U}(\cdot, t) = (\mathbf{v}(\cdot, t), p(\cdot, t), \mathbf{u}(\cdot, t), \mathbf{w}(\cdot, t), q(\cdot, t), r(\cdot, t))^{\top}, \quad (5)$$

for all  $t > 0$ , with an additional initial condition  $\mathbf{U}(\cdot, 0) = \mathbf{U}_0 : \mathbb{R}^d \rightarrow \mathbb{R}^m$  and the associated source term  $\mathbf{F} : \mathbb{R}^d \times [0, +\infty[ \rightarrow \mathbb{R}^m$  being defined as

$$\mathbf{F}(\cdot, t) = (\mathbf{g}(\cdot, t), h(\cdot, t), \mathbf{0}, \mathbf{0}, 0, 0)^{\top}. \quad (6)$$

The evolution problem associated with the augmented system (4) can be written in a compact form as

$$\begin{cases} \frac{\partial}{\partial t} \mathbf{U} + \sum_{j=1}^d \mathbf{A}_j \frac{\partial}{\partial x_j} \mathbf{U} = \mathbf{S} \mathbf{U} + \mathbf{F}, & (\mathbf{x} \in \mathbb{R}^d, t > 0) \\ \mathbf{U}(\mathbf{x}, 0) = \mathbf{U}_0, & (\mathbf{x} \in \mathbb{R}^d) \end{cases} \quad (7)$$

with the only nonzero terms of the matrices  $\mathbf{A}_j$  and  $\mathbf{S}$  of  $\mathcal{M}_m(\mathbb{R})$  being given for  $j = 1, \dots, d$  by

$$[\mathbf{A}_j]_{j, d+1} = \frac{1}{\rho_a} \quad \text{and} \quad [\mathbf{A}_j]_{d+1, j} = \kappa_a,$$

and

$$\begin{cases} [\mathbf{S}]_{j, d+1+j} = -\Omega_{\rho}^2, & [\mathbf{S}]_{d+1, 3d+2} = -\Omega_{\kappa}^2, & [\mathbf{S}]_{d+1+j, j} = 1, \\ [\mathbf{S}]_{d+1+j, 2d+1+j} = -\omega_{\rho}^2, & [\mathbf{S}]_{2d+1+j, d+1+j} = 1, & [\mathbf{S}]_{3d+2, d+1} = 1, \\ [\mathbf{S}]_{3d+2, 3d+2} = -\gamma, & [\mathbf{S}]_{3d+2, 3d+3} = -\omega_{\kappa}^2, & [\mathbf{S}]_{3d+3, 3d+2} = 1, \end{cases}$$

where  $[\mathbf{M}]_{i,j}$  denotes the entry  $(i, j)$  of the matrix  $\mathbf{M}$ . Therefore, in 1D, these matrices read:

$$\mathbf{A}_1 = \begin{pmatrix} 0 & 1/\rho_a & 0 & 0 & 0 & 0 \\ \kappa_a & 0 & 0 & 0 & 0 & 0 \\ 0 & 0 & 0 & 0 & 0 & 0 \\ 0 & 0 & 0 & 0 & 0 & 0 \\ 0 & 0 & 0 & 0 & 0 & 0 \\ 0 & 0 & 0 & 0 & 0 & 0 \end{pmatrix} \quad \text{and} \quad \mathbf{S} = \begin{pmatrix} 0 & 0 & -\Omega_{\rho}^2 & 0 & 0 & 0 \\ 0 & 0 & 0 & 0 & -\Omega_{\kappa}^2 & 0 \\ 1 & 0 & 0 & -\omega_{\rho}^2 & 0 & 0 \\ 0 & 0 & 1 & 0 & 0 & 0 \\ 0 & 1 & 0 & 0 & -\gamma & -\omega_{\kappa}^2 \\ 0 & 0 & 0 & 0 & 1 & 0 \end{pmatrix}.$$

### 2.3. Generalization to multiple resonances

Exploiting the acoustic-electromagnetic analogy (see, e.g., [4, 10]) and building up from references in electromagnetism [46], one could consider the following generalized effective parameters:

$$\hat{\rho}(\omega) = \rho_a \left( 1 - \sum_{\ell=1}^{N_\rho} \frac{\Omega_{\rho,\ell}^2}{\omega^2 - \omega_{\rho,\ell}^2 - i \gamma_{\rho,\ell} \omega} \right), \quad \hat{\kappa}^{-1}(\omega) = \kappa_a^{-1} \left( 1 - \sum_{\ell=1}^{N_\kappa} \frac{\Omega_{\kappa,\ell}^2}{\omega^2 - \omega_{\kappa,\ell}^2 - i \gamma_{\kappa,\ell} \omega} \right). \quad (8)$$

The parameters  $\gamma_{\rho,\ell} \geq 0$  and  $\gamma_{\kappa,\ell} \geq 0$  are dissipation coefficients that account for physical losses, while  $\omega_{\rho,\ell}$ ,  $\omega_{\kappa,\ell}$  denote resonance frequencies. Again, the parameters featured in (8) could be seen as deriving from a homogenization process for an appropriate microstructure. For example, the case of multiple resonant scatterers investigated in [41] yields effective parameters in the form (8).

Following a derivation similar to this of Section 2.2, one can show that the acoustic equations (2) with the frequency-dependent parameters (8) can be recast in the time-domain using a set of additional auxiliary fields  $\mathbf{u}_\ell$ ,  $\mathbf{w}_\ell$  for  $\ell = 1, \dots, N_\rho$  and  $q_\ell$ ,  $r_\ell$  for  $\ell = 1, \dots, N_\kappa$ , which satisfy the following first-order system:

$$\begin{cases} \frac{\partial \mathbf{v}}{\partial t} + \frac{1}{\rho_a} \nabla p + \sum_{\ell=1}^{N_\rho} \Omega_{\rho,\ell}^2 \mathbf{u}_\ell = \mathbf{g}, \\ \frac{\partial p}{\partial t} + \kappa_a \operatorname{div} \mathbf{v} + \sum_{\ell=1}^{N_\kappa} \Omega_{\kappa,\ell}^2 q_\ell = h, \\ \frac{\partial \mathbf{u}_\ell}{\partial t} - \mathbf{v} + \gamma_{\rho,\ell} \mathbf{u}_\ell + \omega_{\rho,\ell}^2 \mathbf{w}_\ell = \mathbf{0}, & (\ell = 1, \dots, N_\rho), \\ \frac{\partial \mathbf{w}_\ell}{\partial t} - \mathbf{u}_\ell = \mathbf{0}, & (\ell = 1, \dots, N_\rho), \\ \frac{\partial q_\ell}{\partial t} - p + \gamma_{\kappa,\ell} q_\ell + \omega_{\kappa,\ell}^2 r_\ell = 0, & (\ell = 1, \dots, N_\kappa) \\ \frac{\partial r_\ell}{\partial t} - q_\ell = 0, & (\ell = 1, \dots, N_\kappa). \end{cases} \quad (9)$$

This augmented system derives from (2) without any approximation and despite being written in terms of  $d(2N_\rho+1)+2N_\kappa+1$  fields overall instead of  $d+1$  only, this approach would remain advantageous numerically. Defining a vector of unknowns by block as

$$\mathbf{U} = (\mathbf{v}, p, \mathbf{u}_1, \dots, \mathbf{u}_{N_\rho}, \mathbf{w}_1, \dots, \mathbf{w}_{N_\rho}, q_1, \dots, q_{N_\kappa}, r_1, \dots, r_{N_\kappa})^\top,$$

with a corresponding source term  $\mathbf{F}$ , then the augmented system (9) can be written in a compact form similar to (7). The forthcoming analysis can in turn be applied to this system.

## 3. Key properties

### 3.1. Matrices and augmented system properties

We focus now on characterizing the properties of the matrices featured in the augmented system (7). Indeed, our purpose is to apply Friedrichs' theory on symmetric hyperbolic systems, see [17] and [13], to prove the well-posedness of the associated initial-value problem. Moreover, some matrices properties will be of prime importance for justifying the implementation of the splitting-based numerical scheme of Section 4.

One starts by elementary properties satisfied by the matrices  $\mathbf{A}_j$  and  $\mathbf{S}$ . Let define for all  $\mathbf{k} \in \mathbb{R}^d$  the matrix  $\mathbf{A}(\mathbf{k})$  as

$$\mathbf{A}(\mathbf{k}) = \sum_{j=1}^d k_j \mathbf{A}_j. \quad (10)$$

Upon defining the notation  $|\mathbf{k}|^2 = \mathbf{k}^\top \mathbf{k}$  as well as  $\sqrt{\cdot}$  as the principal determination of the complex square root such that

$$\sqrt{z} = |z|^{\frac{1}{2}} e^{i \arg z / 2} \quad \text{for } \arg z \in (-\pi, \pi), \quad (11)$$

then it can be checked that the following two properties hold.

**Property 1.** *The matrix  $\mathbf{A}(\mathbf{k})$  is diagonalizable for all  $\mathbf{k} \in \mathbb{R}^d \setminus \{\mathbf{0}\}$  with its spectrum being given by*

$$\text{sp}(\mathbf{A}(\mathbf{k})) = \{0, \pm |\mathbf{k}| c_a\},$$

where 0 is of multiplicity  $3d + 1$ .

**Property 2.** *The spectrum of  $\mathbf{S}$  is given by*

$$\text{sp}(\mathbf{S}) = \left\{0, \Omega^\pm, \pm i \sqrt{\omega_\rho^2 + \Omega_\rho^2}\right\} \quad \text{with} \quad \Omega^\pm = \frac{1}{2} \left(-\gamma \pm \sqrt{\gamma^2 - 4(\omega_\kappa^2 + \Omega_\kappa^2)}\right),$$

where 0 is of multiplicity  $d + 1$  and  $\pm i \sqrt{\omega_\rho^2 + \Omega_\rho^2}$  are each of multiplicity  $d$ . If  $\gamma = 0$ , then all the eigenvalues are purely imaginary. Moreover, if  $\gamma > 0$  then  $\Re(\Omega^\pm) < 0$ .

Next, one introduces the positive-definite diagonal matrix  $\mathbf{E} \in \mathcal{M}_m(\mathbb{R})$  as

$$\mathbf{E} = \text{diag} \left( \{\rho_a\}, \frac{1}{\kappa_a}, \{\rho_a \Omega_\rho^2\}, \{\rho_a \omega_\rho^2 \Omega_\rho^2\}, \frac{1}{\kappa_a} \Omega_\kappa^2, \frac{1}{\kappa_a} \omega_\kappa^2 \Omega_\kappa^2 \right), \quad (12)$$

where the notation  $\{\cdot\}$  stands for diagonal blocks of size  $d$ . If one (or a subset thereof) of the parameters  $\omega_\rho, \omega_\kappa, \Omega_\rho, \Omega_\kappa$  is zero, then the augmented first-order system (4) can be rewritten in terms of a strictly smaller subset of auxiliary fields. The analysis conducted here will be applicable to this new system when the appropriate changes are made. Now, it is checked that the matrix  $\mathbf{E}$  is a symmetrizer for the augmented system (7) in the sense of the following property.

**Property 3.** *For all  $\mathbf{k} \in \mathbb{R}^d \setminus \{\mathbf{0}\}$ , the real matrix  $\mathbf{E}\mathbf{A}(\mathbf{k})$  is symmetric. Moreover, the real matrix  $\mathbf{E}\mathbf{S}$  can be decomposed as*

$$\mathbf{E}\mathbf{S} = \tilde{\mathbf{S}} - \frac{\gamma \Omega_\kappa^2}{\kappa_a} \tilde{\mathbf{I}}_{m-1}$$

where  $\tilde{\mathbf{S}}$  is skew-symmetric and  $\tilde{\mathbf{I}}_{m-1}$  denotes the matrix whose only nonzero term is the diagonal entry  $[\tilde{\mathbf{I}}_{m-1}]_{m-1, m-1} = 1$ .

Lastly, an energy analysis can be performed, see [Appendix A.1](#), to obtain the property below.

**Property 4.** *Let  $\mathbf{U}$  be a solution to the augmented system (7), whose energy at time  $t$  is given by*

$$\mathcal{E}(t) = \frac{1}{2} \int_{\mathbb{R}^d} \mathbf{U}(\mathbf{x}, t)^\top \mathbf{E} \mathbf{U}(\mathbf{x}, t) d\mathbf{x}.$$

The energy writes  $\mathcal{E}(t) = \mathcal{E}_k(t) + \mathcal{E}_p(t)$ , where  $\mathcal{E}_k(t)$  and  $\mathcal{E}_p(t)$  are kinetic and potential energy quantities, respectively given by:

$$\mathcal{E}_k(t) = \frac{1}{2} \int_{\mathbb{R}^d} \rho_a \left( |\mathbf{v}|^2 + \Omega_\rho^2 |\mathbf{u}|^2 + \omega_\rho^2 \Omega_\rho^2 |\mathbf{w}|^2 \right) d\mathbf{x}, \quad \mathcal{E}_p(t) = \frac{1}{2} \int_{\mathbb{R}^d} \frac{1}{\kappa_a} \left( p^2 + \Omega_\kappa^2 q^2 + \omega_\kappa^2 \Omega_\kappa^2 r^2 \right) d\mathbf{x}.$$

Then the total energy satisfies the identity:

$$\frac{d}{dt} \mathcal{E}(t) = - \int_{\mathbb{R}^d} \frac{\gamma \Omega_\kappa^2}{\kappa_a} q^2 d\mathbf{x} + \int_{\mathbb{R}^d} \left( \rho_a \mathbf{v} \cdot \mathbf{g} + \frac{1}{\kappa_a} p h \right) d\mathbf{x}. \quad (13)$$

Since  $\gamma \Omega_\kappa^2 q^2 / \kappa_a \geq 0$ , the above property shows that the augmented system (7) is dissipative unless  $\gamma = 0$ . Indeed, if after a given time  $t$  the external sources vanish, i.e.  $\mathbf{g}(\cdot, t) = \mathbf{0}$  and  $h(\cdot, t) = 0$ , then  $\frac{d}{dt} \mathcal{E}(t) \leq 0$  so that the energy is dissipated.



### 3.2. Well-posedness

We focus now on characterizing the well-posedness of the initial value problem (7) and assessing whether it is stable. To do so, the theory of semigroups and the Hille-Yosida theorem are applicable and they were used in [7] to investigate electromagnetic dispersive waves. See also the approach developed in [37] for Maxwell's equations in dispersive metamaterials. Here, an alternative approach is adopted, based on the existence results by Friedrichs, see [17] and [13], which are relevant to symmetric hyperbolic systems.

The energy analysis provides a proper functional framework for the study of the augmented system (4), namely by using the Hilbert space  $L^2(\mathbb{R}^d)^m$  endowed with the weighted inner product defined by  $\mathbf{E}$ , i.e. for all  $\mathbf{V}, \mathbf{W} \in L^2(\mathbb{R}^d)^m$ :

$$(\mathbf{V}, \mathbf{W})_{L^2(\mathbb{R}^d)^m} = \frac{1}{2} \int_{\mathbb{R}^d} \mathbf{V}(\mathbf{x})^\top \mathbf{E} \mathbf{W}(\mathbf{x}) d\mathbf{x}. \quad (14)$$

Moreover, Property 4 implies that an appropriate norm on  $L^2(\mathbb{R}^d)^m$  to study of the augmented system (7) is the energy norm defined by (14), for which the solution  $\mathbf{U}(\cdot, t) \in L^2(\mathbb{R}^d)^m$  satisfies:

$$\|\mathbf{U}(\cdot, t)\|_{L^2(\mathbb{R}^d)^m} = \mathcal{E}^{\frac{1}{2}}(t).$$

Within this framework, if the source terms are such that  $\mathbf{F}(\cdot, t) \in L^2(\mathbb{R}^d)^m$  for all  $t \geq 0$  then applying the Cauchy-Schwarz inequality to (13) and integrating between  $t > t_0 \geq 0$  yields

$$\|\mathbf{U}(\cdot, t)\|_{L^2(\mathbb{R}^d)^m} \leq \|\mathbf{U}(\cdot, t_0)\|_{L^2(\mathbb{R}^d)^m} + \int_{t_0}^t \|\mathbf{F}(\cdot, \tau)\|_{L^2(\mathbb{R}^d)^m} d\tau. \quad (15)$$

This inequality describes the admissible energy growth for a solution to (7) or, in other words, a stability property for the solution. In particular, this entails that the solution to (7) is unique. Indeed, if  $\mathbf{U}_1, \mathbf{U}_2$  are solutions to (7) with  $\mathbf{U}_1(\cdot, 0) = \mathbf{U}_2(\cdot, 0) = \mathbf{U}_0$  and the same source  $\mathbf{F}$ , then the difference  $\delta\mathbf{U} = \mathbf{U}_1 - \mathbf{U}_2$  satisfies (7) with no source term and a null initial condition. Therefore  $\delta\mathbf{U}$  satisfies (15) with a zero right-hand side term, which implies that  $\delta\mathbf{U}(\cdot, t) = \mathbf{0}$  for all  $t > 0$ .

With the system under consideration being symmetrizable according to Property 3, the theory associated with the so-called class of Friedrichs' symmetric systems can be used now to establish the next result.

**Theorem 3.1.** *The augmented first-order system (7) is a symmetrizable hyperbolic system. If the initial condition  $\mathbf{U}_0$  and the source term  $\mathbf{F}$  satisfy the following smoothness assumptions:*

$$\mathbf{U}_0 \in H^1(\mathbb{R}^d)^m \quad \text{and} \quad \mathbf{F} \in \mathcal{C}^1([0, T]; L^2(\mathbb{R}^d)^m),$$

for  $T > 0$ , then there exists a unique strong solution  $\mathbf{U}$  to the initial value problem (7), and it satisfies

$$\mathbf{U} \in \mathcal{C}^1([0, T]; L^2(\mathbb{R}^d)^m) \cap \mathcal{C}^0([0, T]; H^1(\mathbb{R}^d)^m).$$

*Proof.* See Appendix A.2. □

### 3.3. Dispersion and stability

The dispersion analysis in metamaterials has been described extensively by some authors, see e.g. [6, 46]. Here we only adapt the main results. Let us consider plane-wave solutions to the homogeneous counterpart of (7), i.e. with  $\mathbf{F} = \mathbf{0}$ , of the form

$$\mathbf{U}(\mathbf{x}, t) = \overline{\mathbf{U}} e^{i(\omega t - \mathbf{k} \cdot \mathbf{x})} = \overline{\mathbf{U}} e^{i(\Re(\omega)t - \mathbf{k} \cdot \mathbf{x})} e^{-\Im(\omega)t}, \quad (16)$$

with  $\overline{\mathbf{U}} \in \mathbb{C}^m$ ,  $\omega \in \mathbb{C}$  and the wavevector  $\mathbf{k} \in \mathbb{R}^d$ . Based on (10), one defines the complex perturbation  $\mathbf{A}'(\mathbf{k})$  of  $\mathbf{A}(\mathbf{k})$  by  $\mathbf{S}$  as

$$\mathbf{A}'(\mathbf{k}) = \mathbf{A}(\mathbf{k}) - i\mathbf{S}.$$

There exists nontrivial solutions (16) to (7) provided that

$$\det(\omega \mathbf{I}_d - \mathbf{A}'(\mathbf{k})) = 0, \quad (17)$$

where  $\mathbf{I}_d$  is the identity matrix in  $\mathbb{R}^d$ , so that  $\omega$  is an eigenvalue of the perturbed matrix  $\mathbf{A}'(\mathbf{k}) \in \mathcal{M}_m(\mathbb{C})$ . After straightforward but tedious calculations, one can show that Equation (17) implies the dispersion relation:

$$|\mathbf{k}|^2 = \omega^2 \hat{\rho}(\omega) \hat{\kappa}^{-1}(\omega). \quad (18)$$

Note that (18) coincides with the dispersion relation of the original system (2).

The solution  $\omega$  to (18) depends only on the norm  $|\mathbf{k}|^2 = \mathbf{k}^\top \mathbf{k}$  of the wavevector and this is a consequence of the isotropy of the medium ( $\hat{\rho}$  and  $\hat{\kappa}^{-1}$  being scalars). The phase velocity  $\mathbf{v}_p$  and the group velocity  $\mathbf{v}_g$  are then respectively defined by

$$\mathbf{v}_p(\mathbf{k}) = \omega(|\mathbf{k}|) \frac{\mathbf{k}}{|\mathbf{k}|^2} \quad \text{and} \quad \mathbf{v}_g(\mathbf{k}) = \nabla_{\mathbf{k}} \omega(|\mathbf{k}|).$$

In the inviscid case  $\gamma = 0$ , the parameters  $\hat{\rho}$  and  $\hat{\kappa}^{-1}$  are real and therefore  $\omega^2 \in \mathbb{R}$ . In this case, the following regimes of propagation are found:

- If  $\hat{\rho}(\omega) \hat{\kappa}^{-1}(\omega) < 0$  then  $\omega^2 < 0$  so that  $\Im(\omega) < 0$  according to (11). The waves are evanescent in time, which corresponds to a band-gap (BG).
- If  $\hat{\rho}(\omega) < 0$  and  $\hat{\kappa}^{-1}(\omega) < 0$  then  $\mathbf{v}_p(\mathbf{k}) \cdot \mathbf{v}_g(\mathbf{k}) < 0$ , which yields backward propagating waves. This property relies on the fact that  $\hat{\rho}$  and  $\hat{\kappa}^{-1}$  satisfy the *growing property* defined in [6], which is the case for the constitutive parameters (3) considered. In these so-called negative index materials (NIM), negative refraction is obtained in 2D and 3D, see [20].
- The case  $\hat{\rho}(\omega) > 0$  and  $\hat{\kappa}^{-1}(\omega) > 0$  corresponds to double-positive materials (DPM), which are characterized by usual propagative and dispersive behaviors.

The stability of the initial value problem (7) is already encapsulated in the energy estimate (15). However, to justify the ensuing numerical scheme, we provide here a complementary analysis that makes use of the properties of the matrix  $\mathbf{S}$ .

**Property 5.** *The initial value problem (7) is stable. Moreover, the associated augmented first-order system (7) is nondissipative when  $\gamma = 0$ .*

*Proof.* See Appendix A.3. □

### 3.4. Interfaces conditions

In this section, we focus on establishing transmission conditions for the augmented hyperbolic system (7). Starting from the identity (A.2), we consider a domain  $\mathcal{D} \subset \mathbb{R}^d$  composed of two open subsets  $\mathcal{D}_1$  and  $\mathcal{D}_2$  that satisfy

$$\overline{\mathcal{D}} = \overline{\mathcal{D}_1} \cup \overline{\mathcal{D}_2}, \quad \mathcal{D}_1 \cap \mathcal{D}_2 = \emptyset, \quad \partial \mathcal{D}_1 \cap \partial \mathcal{D}_2 = \Gamma, \quad \partial \mathcal{D}_1 \cup \partial \mathcal{D}_2 = \Gamma \cup \Gamma_c,$$

so that  $\Gamma$  denotes the interface between these two subdomains while the complementary part  $\Gamma_c$  is possibly empty. Each of the subdomains is endowed with specific materials properties that yield, for  $i = 1, 2$ , the corresponding matrices  $\mathbf{E}^{(i)}$ ,  $\mathbf{A}_j^{(i)}$  and  $\mathbf{S}^{(i)}$ . Moreover, for the sake of argument, let assume no material damping, i.e.  $\gamma^{(1)} = \gamma^{(2)} = 0$  and no external sources, i.e.  $\mathbf{F}^{(1)} = \mathbf{F}^{(2)} = \mathbf{0}$ . According to Theorem 3.1, the solutions  $\mathbf{U}^{(i)}$  with  $i = 1, 2$  to the corresponding initial value problem (7) in each subdomain satisfy

$$\mathbf{U}^{(i)} \in \mathcal{C}^1([0, +\infty[; L^2(\mathcal{D}_i)^m) \cap \mathcal{C}^0([0, +\infty[; H^1(\mathcal{D}_i)^m).$$

When the complementary part  $\Gamma_c$  of the domain boundary is at infinity, then concatenating the two energy identities (A.2) corresponding to  $\mathcal{D}_1$  and  $\mathcal{D}_2$  entails

$$\begin{aligned} \frac{1}{2} \frac{d}{dt} \int_{\mathcal{D}_1} \mathbf{U}^{(1)\top} \mathbf{E}^{(1)} \mathbf{U}^{(1)} d\mathbf{x} + \frac{1}{2} \frac{d}{dt} \int_{\mathcal{D}_2} \mathbf{U}^{(2)\top} \mathbf{E}^{(2)} \mathbf{U}^{(2)} d\mathbf{x} \\ + \frac{1}{2} \int_{\Gamma} \left\{ \mathbf{U}^{(1)\top} \mathbf{E}^{(1)} \mathbf{A}^{(1)}(\mathbf{n}) \mathbf{U}^{(1)} - \mathbf{U}^{(2)\top} \mathbf{E}^{(2)} \mathbf{A}^{(2)}(\mathbf{n}) \mathbf{U}^{(2)} \right\} d\mathbf{s} = 0, \end{aligned}$$

using the unit outward normal  $\mathbf{n}_1 = -\mathbf{n}_2$  to  $\mathcal{D}_1$  as the reference normal  $\mathbf{n}$ . The requirement that energy is conserved entails that the following condition has to be satisfied on the interface  $\Gamma$ :

$$\llbracket \mathbf{U}^\top \mathbf{E} \mathbf{A}(\mathbf{n}) \mathbf{U} \rrbracket = \mathbf{0}, \quad (19)$$

where the double-bracket notation denotes jumps across  $\Gamma$ , i.e.  $\llbracket f \rrbracket = f^{(2)} - f^{(1)}$ . Given the definitions of the matrices  $\mathbf{E}$  and  $\mathbf{A}(\mathbf{n})$ , and using the identity  $\llbracket fg \rrbracket = \llbracket f \rrbracket \langle g \rangle + \langle f \rangle \llbracket g \rrbracket$  where  $\langle f \rangle = \frac{1}{2}(f^{(2)} + f^{(1)})$ , then a sufficient condition for equation (19) to hold is that the following transmission conditions are satisfied at the interface:

$$\llbracket \mathbf{v} \cdot \mathbf{n} \rrbracket = \mathbf{0} \quad \text{and} \quad \llbracket p \rrbracket = 0. \quad (20)$$

It is noticeable that, despite the introduction of auxiliary fields that led to the augmented system (7), the associated transmission conditions at an interface can be reduced to these of the original acoustic equations.

## 4. Numerical modeling

### 4.1. Splitting

A numerical scheme is proposed to compute the solution to the augmented system (7). Introducing a uniform Cartesian grid with mesh size  $\Delta x$  and time step  $\Delta t$ , let  $\mathbf{U}_{j_1, \dots, j_d}^n$  denote the approximation of the solution at the point  $\mathbf{x} = (j_1 \Delta x, \dots, j_d \Delta x)$  and time  $t = n \Delta t$ . A straightforward discretization of (7) typically leads to the following numerical CFL stability condition

$$\Delta t \leq \min \left( \frac{\Delta x}{c_a}, \frac{2}{\varrho(\mathbf{S})} \right) \quad (21)$$

where  $\varrho(\mathbf{S})$  denotes the spectral radius of  $\mathbf{S}$ . As shown by Property 2, the usual CFL bound on the time step, i.e.  $\Delta t \leq \Delta x / c_a$ , could be much reduced for some values of the parameters featured in the matrix  $\mathbf{S}$ , which would in turn be detrimental to performances of the numerical scheme.

To circumvent this issue, we follow here the Strang splitting approach analyzed in [25]. To implement (7) numerically, the augmented hyperbolic system is split into a propagative part and a relaxation part as follows:

$$\begin{cases} \frac{\partial}{\partial t} \mathbf{U} + \sum_{j=1}^d \mathbf{A}_j \frac{\partial}{\partial x_j} \mathbf{U} = \mathbf{0}, & (22a) \\ \frac{\partial}{\partial t} \mathbf{U} = \mathbf{S} \mathbf{U} + \mathbf{F}. & (22b) \end{cases}$$

These two equations are in turn intended to be solved alternatively. The discrete operators associated with the discretizations of (22a) and (22b) are respectively denoted by  $\mathcal{P}_\alpha$  and  $\mathcal{R}_\beta[t]$  with  $\alpha$  and  $\beta$  being some parameters associated with the time-domain discretization. The operator  $\mathcal{R}_\beta[t]$  depends explicitly on time when the forcing term  $\mathbf{F}$  is nonzero, whereas  $\mathcal{P}_\alpha$  remains independent on  $t$ . Following [25], then the split equations (22a) and (22b) are solved with adequate time increments according to the following scheme:

**Algorithm 1 (Splitting algorithm).**

$$\begin{array}{ll} \text{Initialize :} & \mathbf{U}^n = \mathbf{U}_0 \\ \text{Iterate for } n \geq 1 : & \begin{cases} \mathbf{U}^* &= \mathcal{R}_{\Delta t/2}[t_n] \mathbf{U}^n \\ \mathbf{U}^{**} &= \mathcal{P}_{\Delta t} \mathbf{U}^* \\ \mathbf{U}^{n+1} &= \mathcal{R}_{\Delta t/2}[t_{n+1}] \mathbf{U}^{**} \end{cases} \end{array}$$

Note that the spatial indices are omitted for brevity so that the fields featured in the above algorithm concatenate the unknowns at all points of the computational grid. Since the matrices  $\mathbf{A}_j$  and  $\mathbf{S}$  do not commute, an error associated with the splitting scheme is introduced, as shown in [25]. However, provided that  $\mathcal{P}_\alpha$  and  $\mathcal{R}_\beta$  are associated with numerical schemes that are at least second-order accurate and stable, then the time-marching Algorithm 1 constitutes a second-order approximation of the original evolution problem (7).

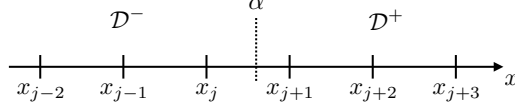


Figure 1: Finite-difference grid and interface separating two domains  $\mathcal{D}^-$  and  $\mathcal{D}^+$  at  $x = \alpha$ .

#### 4.2. Numerical scheme

In this section, we describe the discrete operators featured in Algorithm 1.

**Relaxation step.** The physical parameters do not vary with time so that the matrix  $\mathbf{S}$  is constant in time. Accordingly, for  $\beta > 0$ , one defines the discrete relaxation operator as:

$$\mathcal{R}_\beta[t] \mathbf{U} = e^{\beta \mathbf{S}} (\mathbf{U} + \beta \mathbf{F}(t)). \quad (23)$$

If there is no excitation (i.e.  $\mathbf{g} = \mathbf{0}$  and  $h = 0$ ), then (23) is exact. The matrix exponential entering the definition of  $\mathcal{R}_\beta[t]$  is computed in a pre-processing step using the method 2 in [36] based on a (6/6)-Padé approximation. Property 2 ensures that the computation of this exponential is stable.

**Propagation step.** To integrate (22a), we use a fourth-order ADER (Arbitrary DERivative) scheme [43]. This explicit two-step and single-grid finite-difference scheme defines the discrete propagation operator formally as:

$$(\mathcal{P}_{\Delta t} \mathbf{U})_{j_1, \dots, j_d} = \mathbf{U}_{j_1, \dots, j_d} - \sum_{\ell_1=-2}^{+2} \dots \sum_{\ell_d=-2}^{+2} \mathbf{C}_{\ell_1, \dots, \ell_d} \mathbf{U}_{j_1+\ell_1, \dots, j_d+\ell_d}. \quad (24)$$

The matrices  $\mathbf{C}_{\ell_1, \dots, \ell_d}$  defining the scheme (24) are provided in Section 4 of [2] in the cases  $d = 1$  and  $d = 2$  while they can be generalized in a straightforward manner to the case  $d = 3$ . The ADER-4 scheme employed here satisfies the following CFL stability condition independently of the dimension  $d$ , i.e.

$$\Delta t \leq \frac{\Delta x}{c_a}. \quad (25)$$

Noticeably, the stability condition (25) resulting from the splitting approach is *optimal* in the sense that, contrary to condition (21), it coincides with the CFL condition of classical acoustics.

#### 4.3. Interface discretization

Notoriously, interfaces are detrimental to the quality of finite-difference methods, for three main reasons: (i) errors of order  $\mathcal{O}(\Delta x)$  are introduced when the interfaces do not coincide with the mesh, and a naive stair-step description of the geometries results in spurious diffractions; (ii) jump conditions are not properly enforced by usual finite-difference schemes; (iii) solutions are not smooth across interfaces, which lowers the convergence order of the method or even leads to numerical instabilities. To remove these difficulties, while keeping the advantages of using a Cartesian grid, the so-called immersed interface method is implemented, see [30, 32] and the references therein for details and analysis. For the sake of simplicity, the principle is exposed below in 1D.

For a given finite-difference scheme, one defines *irregular* points as the points where the associated spatial stencil intersects an interface. For example, consider two subdomains  $\mathcal{D}^-$  and  $\mathcal{D}^+$  with their interface being located at  $x = \alpha$ , see Figure 1, and the fourth-order ADER scheme expressed at the point  $x_j \in \mathcal{D}^-$ . The stencil being of width 2 then the irregular points are the points  $\{x_{j-2}, x_{j-1}, x_j, x_{j+1}, x_{j+2}\}$  of Figure 1. The other grid points are *regular* points. While the relaxation operator  $\mathcal{R}_\beta[t]$  of Section 4.2 remains unchanged, the propagation operator  $\mathcal{P}_\alpha$  is modified at those irregular points. Namely, instead of using in (24) the numerical values  $\mathbf{U}_{j+\ell}$  with  $\ell = -2, \dots, 2$ , the new scheme involves some modified values  $\mathbf{U}_{j+1}^\sharp$  and  $\mathbf{U}_{j+2}^\sharp$  at the irregular points  $x_{j+1}$  and  $x_{j+2}$  of  $\mathcal{D}^+$ . These modified values  $\mathbf{U}_{j+\ell}^\sharp$  are constructed as smooth extensions

of  $\mathbf{U}_{j+l}$  across the interface relatively to the point  $x_j \in \mathcal{D}^-$ . Doing so, the modified propagation scheme at that point uses the quantities  $\{\mathbf{U}_{j-2}, \mathbf{U}_{j-1}, \mathbf{U}_j, \mathbf{U}_{j+1}^\#, \mathbf{U}_{j+2}^\#\}$ . Note that, in the schematics of Figure 1, the interface is placed at the off-grid point  $x = \alpha$  to emphasize the fact that the geometry of the interface can be described independently of the mesh, i.e., it may or may not coincide with grid points. In particular, in the numerical experiments presented hereafter, the interfaces are placed at off-grid points to illustrate the subcell resolution offered by the immersed interface method.

As shown in Section 3.4, the interface conditions (20) coincide with those of classical acoustics. Consequently, it is straightforward to adapt the strategy proposed in [30, 32] for the computation of the modified grid values.

## 5. Numerical experiments

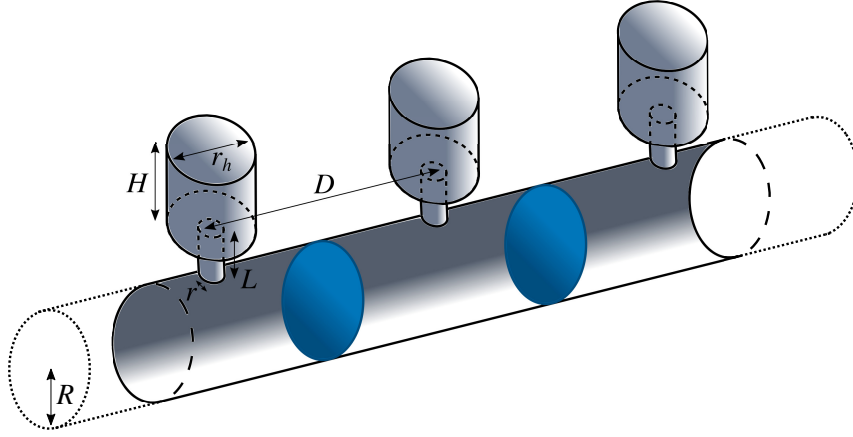


Figure 2: Array of Helmholtz resonators with interspaced elastic membranes (in blue).

### 5.1. Case study

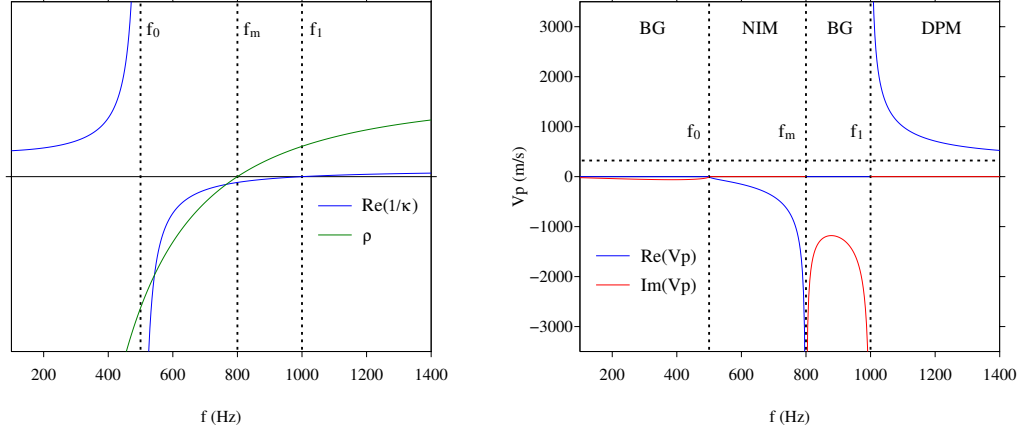
Here we investigate a simple 1D configuration that can be modeled within the framework of Section 2.1. Consider an infinite cylindrical tube that is periodically connected with cylindrical Helmholtz resonators (HRs) and contains equi-spaced elastic membranes (Figure 2). Radius of the tube is  $R$ , axial spacing between resonators is  $D$ , radius and length of HRs neck are  $r$  and  $L$ , radius and height of the HRs cavity are  $r_h$  and  $H$ . Therefore the cross-sectional area of the tube is  $S = \pi R^2$  and that of HRs neck is  $A = \pi r^2$  while their volume is  $V = \pi r_h^2 H$ . One defines the parameter  $\omega_\kappa$  as the resonance frequency of the resonators and one introduces the parameter  $\Omega_\kappa$  so that  $\sqrt{\omega_\kappa^2 + \Omega_\kappa^2}$  is the resonance frequency of the tube coupled with the resonators. These parameters satisfy [14]:

$$\omega_\kappa = c_a \sqrt{\frac{A}{LV}} := 2\pi f_0, \quad \Omega_\kappa = \omega_\kappa \sqrt{\frac{V}{SD}} := 2\pi f_1, \quad (26)$$

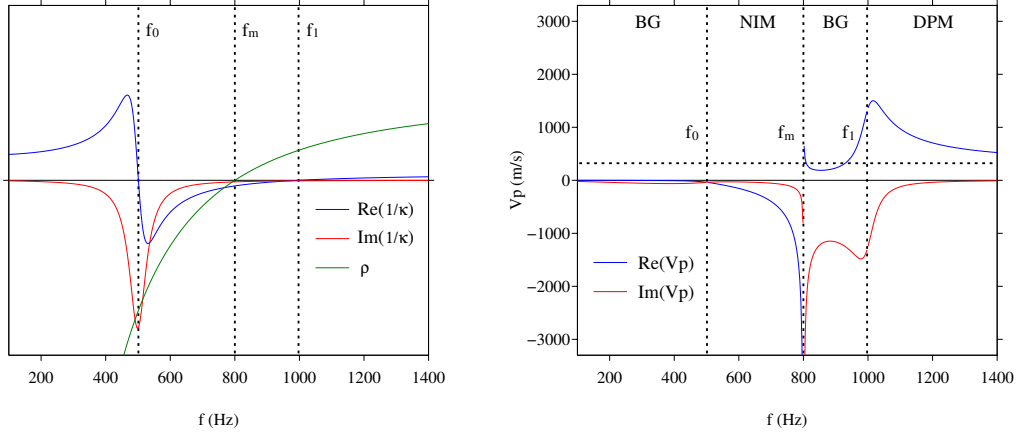
The elastic membranes have stiffness  $K$  and mass  $M$ . The average density of the fluid loaded with the membrane in the tube is  $\rho_m > \rho_a$ , so that the resonance frequency of the membranes is:

$$\Omega_\rho = \sqrt{\frac{K}{\rho_m}} := 2\pi f_m. \quad (27)$$

This system is driven in such a way that wave propagation is linear and occurs in the sub-wavelength regime ( $c_a/\omega \gg D$ ). Moreover, in order to excite only the first plane-wave mode of the tube, one must



(a) Inviscid case ( $\gamma = 0$ ). The curve  $\Im\{\hat{\kappa}^{-1}\} = 0$  is not shown in left panel.



(b) Dissipative case ( $\gamma = 400 \text{ s}^{-1}$ ).

Figure 3: [Left: Scaled curves of  $\hat{\rho}$  and  $\hat{\kappa}^{-1}$  in (3)]. [Right: Phase velocity]. Horizontal dotted line coincide with the value of the classical sound velocity  $c_a$ . Vertical dotted lines separate the frequency domain into intervals where occur the following phenomena: band-gap (BG), negative index material (NIM), and double-positive material (DPM). Numerical values of the parameters are summarized in Table 1

satisfy approximately the condition  $\omega < 1.84 c_a/R$ , according to the cut-off frequency value given in [8]. Doing so, the 1D approximation is valid [31]. Under these assumptions, when the system considered is homogenized then the effective parameters correspond to the frequency dependent laws (3a) and (3b) with  $\omega_\rho = 0$  as shown in [44, 24, 20].

The chosen numerical values of the parameters are provided in Table 1 while  $\rho_a$  and  $c_a$  are the standard values for air. The membrane stiffness and geometrical parameters of the HRs are tuned so as to yield sufficiently large frequency intervals of existence for the band-gap and negative index material behaviors, i.e.  $f_0 = 500$  Hz,  $f_1 = 1000$  Hz and  $f_m = 800$  Hz in (26) and (27). Note that, in particular, these parameter values are based on the experimental values reported in [23]. For this choice of parameters, the material laws (3) and the associated propagation regimes described in Section 3.3 based on the dispersion relation (18) are shown in Figure 3. For this configuration, one thus has  $\omega_\rho = 0$  while  $\omega_\kappa \neq 0$ ,  $\Omega_\kappa \neq 0$  and  $\Omega_\rho \neq 0$  and the numerical values of the latter three coefficients being such that they make it possible to observe all relevant wave phenomena given the excitation signal considered in the following section.

$c_a$ (m s <sup>-1</sup> )	$\rho_a$ (kg m <sup>-3</sup> )	$\rho_m$ (kg m <sup>-3</sup> )	$K$ (N m <sup>-4</sup> )	$\gamma$ (s <sup>-1</sup> )	$A/LV$ (m <sup>-2</sup> )	$V/S D$
345	1.17	1.34	$3.38 \cdot 10^7$	0 or 400	1.45	3

Table 1: Physical and geometrical parameters for the studied configuration.

### 5.2. One-dimensional homogeneous medium

The chosen propagation domain  $[-5\text{m}, 5\text{m}]$  is discretized using 1000 nodes. This implies that the wavelength at 2 kHz is sampled on 16 nodes, which yields a relative error on the phase velocity lower than 0.0056% [30]. The time step is chosen so as to satisfy the CFL condition (25) with a 0.95 threshold. The simulations are stopped before the waves reach the edges of the computational domain, so that no outgoing condition is required; PMLs for dispersive media are not treated here and require special treatments, see [46].

An excitation is applied to the momentum equation at the point  $x_s = 0$  such that  $g(x, t) = \delta(x - x_s) G(t)$  and  $h = 0$  in (6), with the time-domain signal  $G(t)$  being defined as follows:

$$G(t) = \begin{cases} \sum_{m=1}^4 a_m \sin(\beta_m \omega_c t) & \text{if } 0 < t < \frac{1}{f_c}, \\ 0 & \text{otherwise,} \end{cases} \quad (28)$$

where  $\beta_m = 2^{m-1}$  and the coefficients  $a_m$  being  $a_1 = 1$ ,  $a_2 = -21/32$ ,  $a_3 = 63/768$ ,  $a_4 = -1/512$ , which entails the smoothness property  $G \in C^6([0, +\infty[)$ . As shown Figure 4, so defined,  $G(t)$  is a wide-band signal with a central frequency  $f_c = \omega_c/2\pi = 700$  Hz that lies in the NIM region indicated on Figure 3.

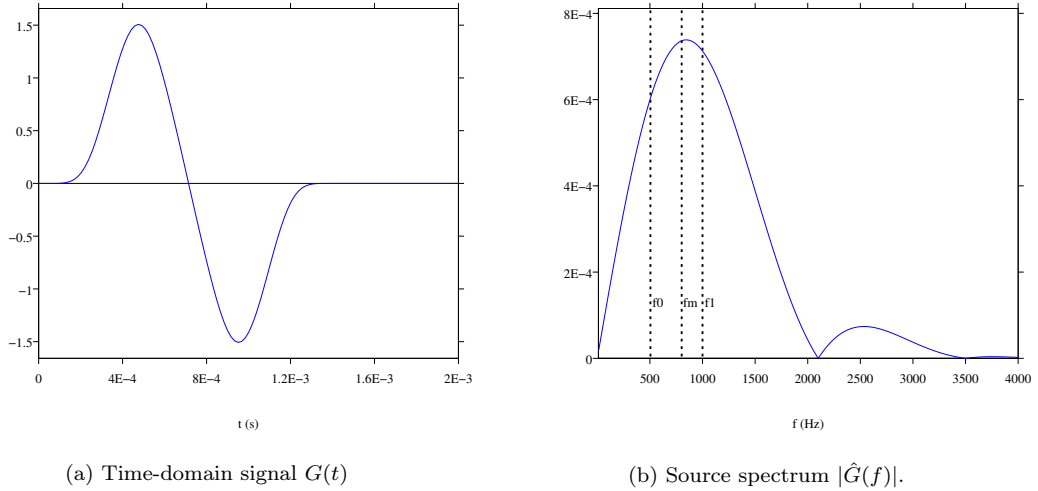


Figure 4: Wide-band function  $G$  used as the excitation signal in the 1D numerical experiment.

For comparison, a reference semianalytical solution is computed by applying time and space Fourier transforms to (4). With  $\hat{f}$  the Fourier transform of  $f$ , then the residue theorem yields identities in the Fourier domain such as

$$\hat{p}(x, \omega) = \text{sign}(x - x_s) \rho_a e^{-ik(\omega)|x-x_s|} \hat{G}(\omega), \quad (29)$$

for the pressure field and similarly for the other fields. In (29),  $k(\omega)$  is the wavenumber that satisfies the dispersion relation (18). Inspection of (18) and (3) shows that  $k(\omega)$  has singularities depending on the value of the dissipative coefficient  $\gamma$ . Some care must therefore be taken to compute the inverse Fourier transform of (29). For this purpose, the integrable singularities such as  $1/\sqrt{\omega - \Omega_\rho}$  are taken into account analytically by using appropriate changes of variables. Outside singularities, a midpoint quadrature formula

with automatic refinement is implemented [16]. Doing so, the solution to (4) is finally computed in the time domain by taking the real part of the inverse Fourier transform of (29).

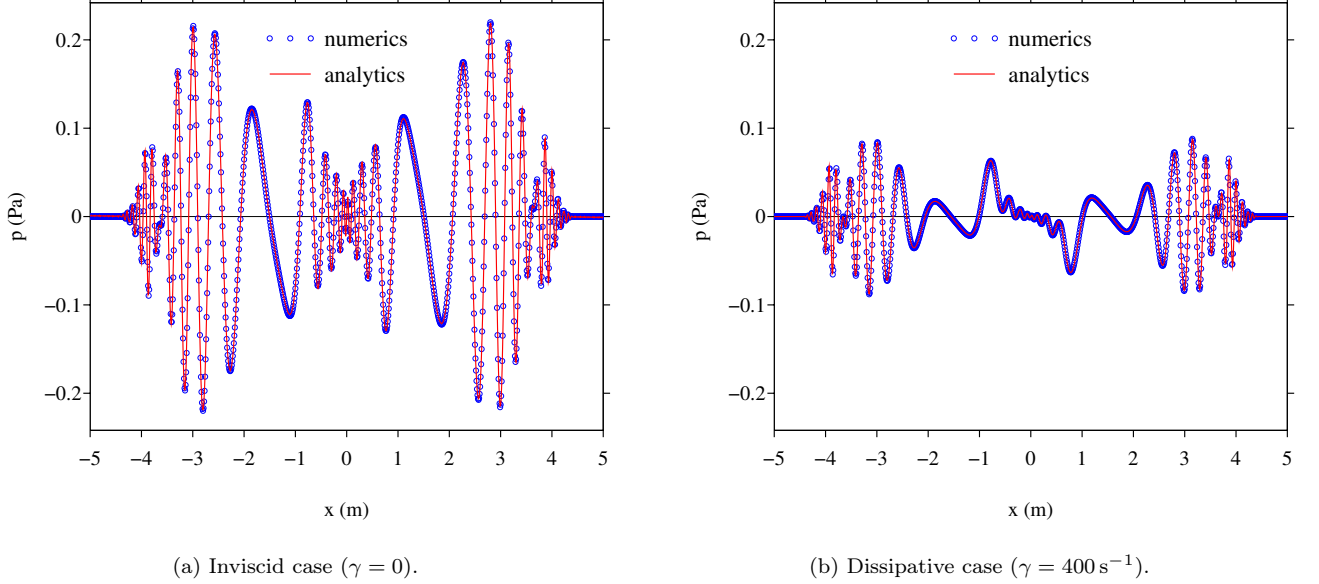


Figure 5: Snapshots of acoustic pressure  $p$  at  $t = 14$  ms in the homogeneous metamaterial domain.

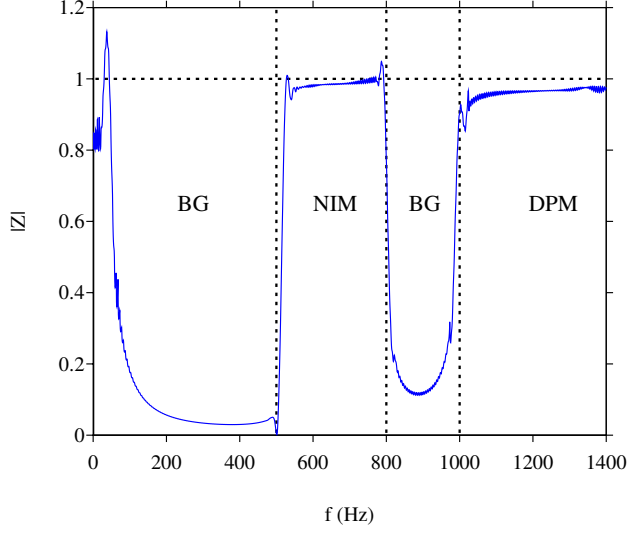
Figure 5 displays snapshots of the acoustic pressure  $p$  at time  $t = 14$  ms for  $\gamma \in \{0, 400\} \text{ s}^{-1}$ . Very good agreement is found between the numerical solutions computed using the numerical scheme of Section 4 and the corresponding semianalytical ones. The effect of attenuation is clearly seen with decrease of amplitude when  $\gamma = 400 \text{ s}^{-1}$ . The frequency content of the source around  $f_c$  yields backward propagating waves towards  $x_s$  in a typical NIM behavior. The observed high-frequency propagating waves correspond to DPM behavior. The noticeable small amplitude of these waves is a consequence of the weak energy content of the source at the corresponding frequencies. Lastly, it should be noted that the existence of resonance frequencies, i.e. singularities, in the material laws (3) do not impede the computation of smooth  $L^2$  transient solutions in such time-domain simulations with broad frequency-band sources. Such a remarkable property of the proposed time-domain approach is assessed by Theorem 3.1.

Based on the large frequency content of the source signal (28) one can identify the various propagation regimes in a single time-domain experiment. For this purpose, one must measure the transmission spectrum that characterizes the medium considered. The velocity field  $v(x, t)$  computed numerically is measured at the source  $x_s$  and at a receiver location  $x_r = 0.5 \text{ m}$  for  $t \in [0, 0.2 \text{ s}]$ . Then the sought transmission spectrum is defined as the modulus  $|Z(\omega)| = |\hat{v}(x_r, \omega)/\hat{v}(x_s, \omega)|$ , expressed in terms of the Fourier transforms of the acquired data. Note that, to avoid spurious reflections at the boundary of the computational domain, the latter is extended up to  $[-20 \text{ m}, 20 \text{ m}]$  and meshed using 4000 nodes. Figure 6 displays the computed transmission spectrum. In the inviscid case, the transmission coefficient is close to 1 in the frequency ranges of NIM and DPM as expected. In the BG ranges,  $|Z|$  decreases to 0. In the dissipative case, attenuation is observed in the NIM and DPM ranges due to the intrinsic material attenuation.

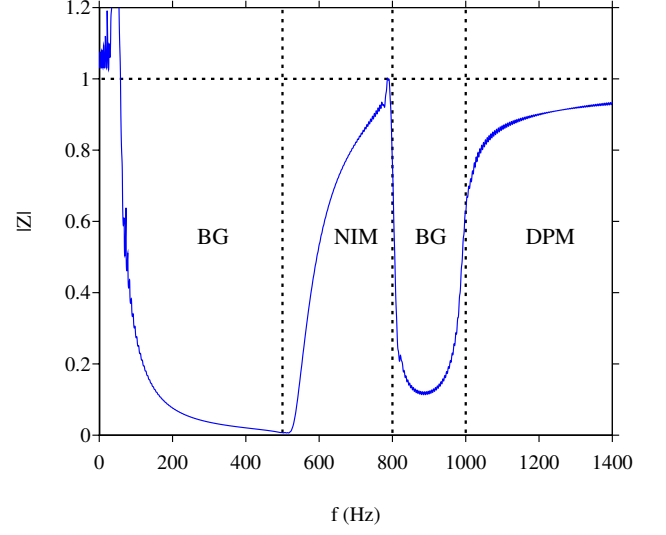
### 5.3. One-dimensional interface problems

In this section one focuses on numerical results for interface problems. In the first example of Figure 7, an interface is introduced at the off-grid point  $\alpha = 6.5 \cdot 10^{-2} \text{ m}$  to separate a fluid domain  $\mathcal{D}_1 = \{x; x < \alpha\}$  and a metamaterial domain  $\mathcal{D}_2 = \{x; x > \alpha\}$ . Note that the interface does not coincide with a node of



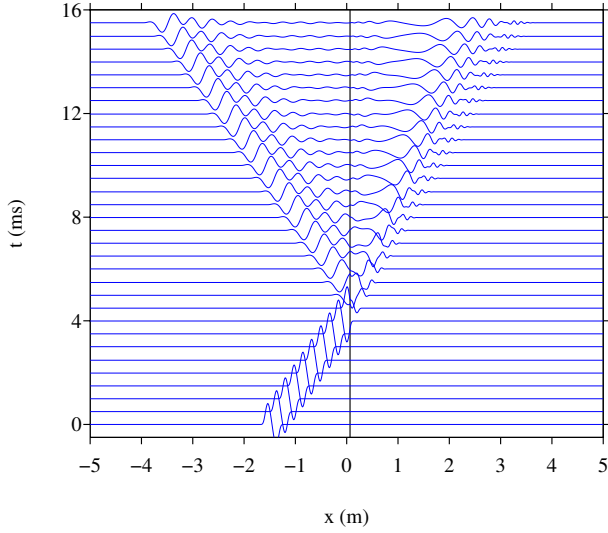


(a) Inviscid case ( $\gamma = 0$ ).

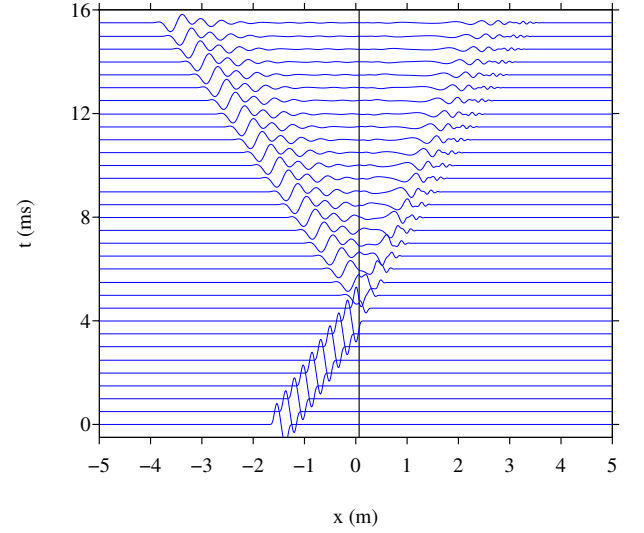


(b) Dissipative case ( $\gamma = 400 \text{ s}^{-1}$ ).

Figure 6: Transmission spectrum computed numerically. Vertical dotted lines separate the theoretical propagation regimes. Horizontal dotted lines denote perfect transmission  $|Z| = 1$ .



(a) Inviscid case ( $\gamma = 0$ ).

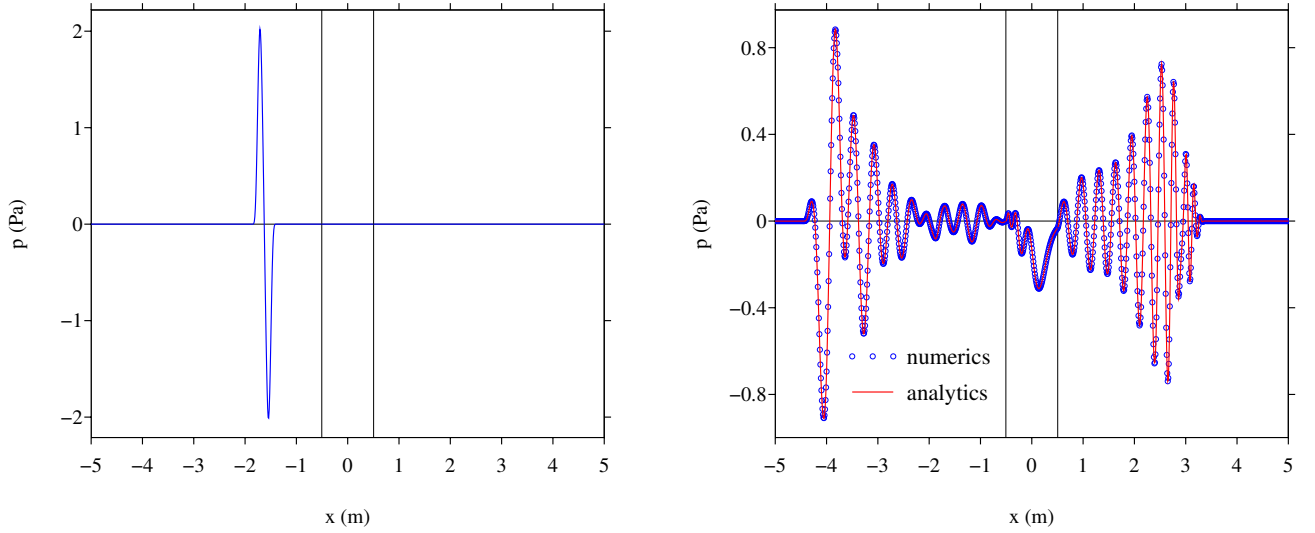


(b) Dissipative case ( $\gamma = 400 \text{ s}^{-1}$ ).

Figure 7: Seismogram of the acoustic pressure  $p$  for the fluid-metamaterial interface problem. Vertical line denotes the material interface.

the discretization grid and the jump conditions (20) are implemented using the immersed interface method described in Section 4.3. The fluid is air, with density  $\rho^{(1)} = 1.17 \text{ kg m}^{-3}$  and sound speed  $c^{(1)} = 345 \text{ m s}^{-1}$ , while the acoustic metamaterial is that described in the previous section.

The set of auxiliary fields and the affiliated augmented system (4) are used only in the metamaterial domain while the classical acoustic system (1) is solved in the fluid domain. Accordingly, the computation is initialized by an initial condition defined as  $\mathbf{U}_0(x) = (-1/c^{(1)}, \rho^{(1)})^\top G(t_0 - \frac{x}{c^{(1)}})$  with  $t_0 = -4 \text{ ms}$ , which is compactly supported within the fluid. This condition is designed so as to generate a right-going wave. Figure 7 displays seismograms of the pressure field  $p$ , with and without attenuation. The reflected waveform in  $\mathcal{D}_1$  can be thought to be surprising since the fluid domain is not dispersive. In fact, this behavior is a consequence of the frequency dependence of the reflection coefficient at the fluid-metamaterial interface. Moreover, in the domain  $\mathcal{D}_2$ , the observed waveform is induced by backward propagating transmitted waves within the frequency interval of the NIM regime, which generate waves reflected back at the interface.



(a) Initial pressure condition.

(b) Pressure field  $p$  at  $t = 14 \text{ ms}$  ( $\gamma = 0$ ).

Figure 8: Wave propagation within a fluid-metamaterial-fluid medium.

In the second example of Figure 8, a fluid-metamaterial-fluid medium is considered with two interfaces at the off-grid points  $\alpha_1 = -5.05 \cdot 10^{-1} \text{ m}$  and  $\alpha_2 = +5.05 \cdot 10^{-1} \text{ m}$ . The fluid subdomains surrounding the acoustic metamaterial are endowed with the properties of air while the metamaterial is defined as previously with  $\gamma = 0$ . Figure 8a shows the initial condition and a snapshot of the pressure field  $p$  at time  $t = 14 \text{ ms}$  is shown Fig. 8b. Very good agreement is found between the numerical solution and the semianalytical one.

#### 5.4. Two-dimensional scattering

Figure 9 depicts the acoustic version of the Pendry-Veselago lens. Two media characterized by a positive acoustic index  $n = 1$  surround a slab of negative acoustic index  $n < 0$ . In such a configuration, a time-harmonic point source placed on one side of the slab focuses perfectly at a single point on the other side [10]. To illustrate this phenomenon, we consider the domain  $[-4, 4] \times [-4, 4] \text{ m}^2$  which is discretized using a grid of  $800 \times 800$  points. In the configuration of Figure 10, two interfaces surround a metamaterial slab which has the properties given in Table 1. The surrounding medium is air so that this example is a 2D version of the 1D example of Figure 8. Propagation in an infinite domain is simulated by using Perfectly-Matched Layers (PMLs) at the boundary of the computational domain. PMLs are used only within the fluid regions. Special dispersive PMLs are required within the metamaterial: the existence of backward waves (for which

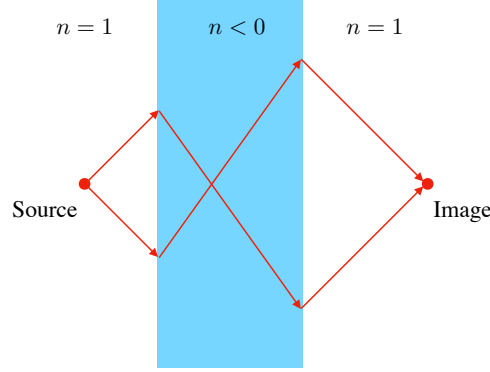


Figure 9: Acoustic lens via negative refraction: schematics depicting the focusing of rays.

the group and phase velocities have opposite directions) in negative-index metamaterial makes classical PML unstable, see [46] and the references therein.

The source at  $\mathbf{x}_s = (-1.532, -1.285)$  m is time-harmonic with frequency  $f_c = 678.57$  Hz. Figure 10 displays the pressure field  $p$  in two configurations after a sufficiently long time, here  $t = 60$  ms. Figure 10a corresponds to a perfect flat lens resulting from the negative index of refraction  $n = -1$  within the metamaterial slab as predicted theoretically, see [10]. Figure 10b illustrates the simulation of the behavior of the lens in a geometrically perturbed configuration. Moreover, this example illustrates that the proposed Cartesian grid finite-difference scheme can handle efficiently geometries that are non conforming to the mesh.

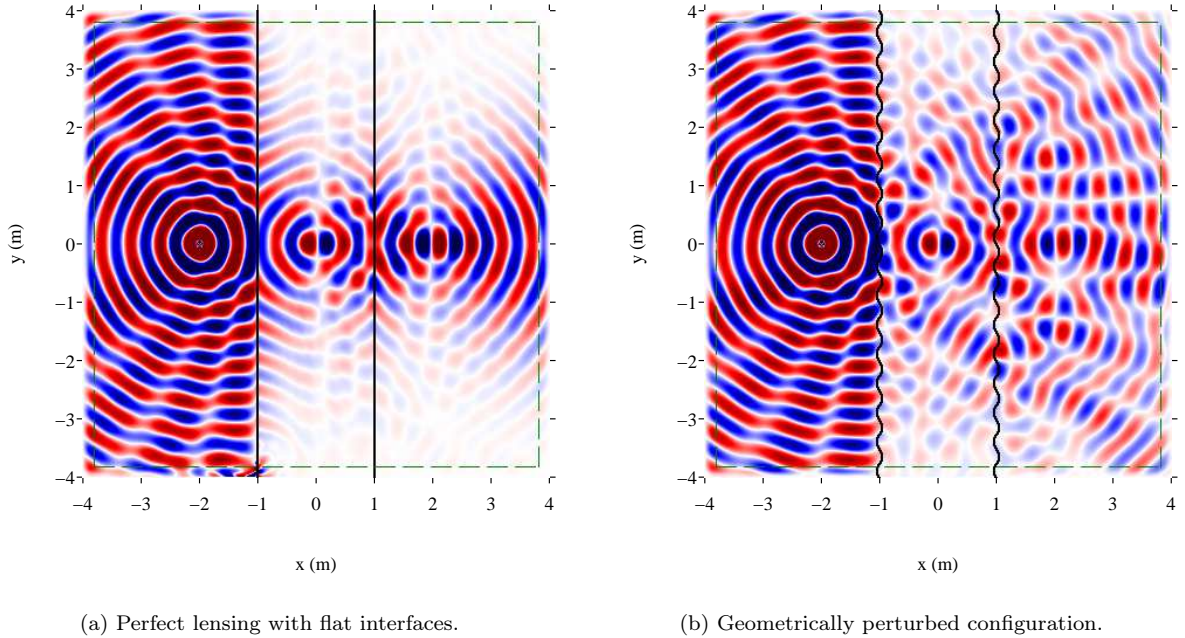


Figure 10: Snapshots of pressure field  $p$  at time  $t = 60$  ms in a 2D layered fluid-metamaterial-fluid domain given a time-harmonic excitation at  $f_c = 678.57$  Hz. The refraction indices of are  $n = +1$  within the fluid and  $n = -1$  in the metamaterial.

Figure 11 corresponds to the transient simulation of the scattering by two metamaterial obstacles for a time-harmonic source at  $f_c = 800$  Hz placed at the origin. The obstacles material parameters are tuned so

that the bottom one exhibits a stop-band behavior at the source frequency. For this time-domain simulation, Fig. 11a illustrates that the pressure is nonzero in the bottom obstacle at the onset of the excitation while the band-stop behavior occurs after a sufficiently long time, as seen in Fig. 11b.

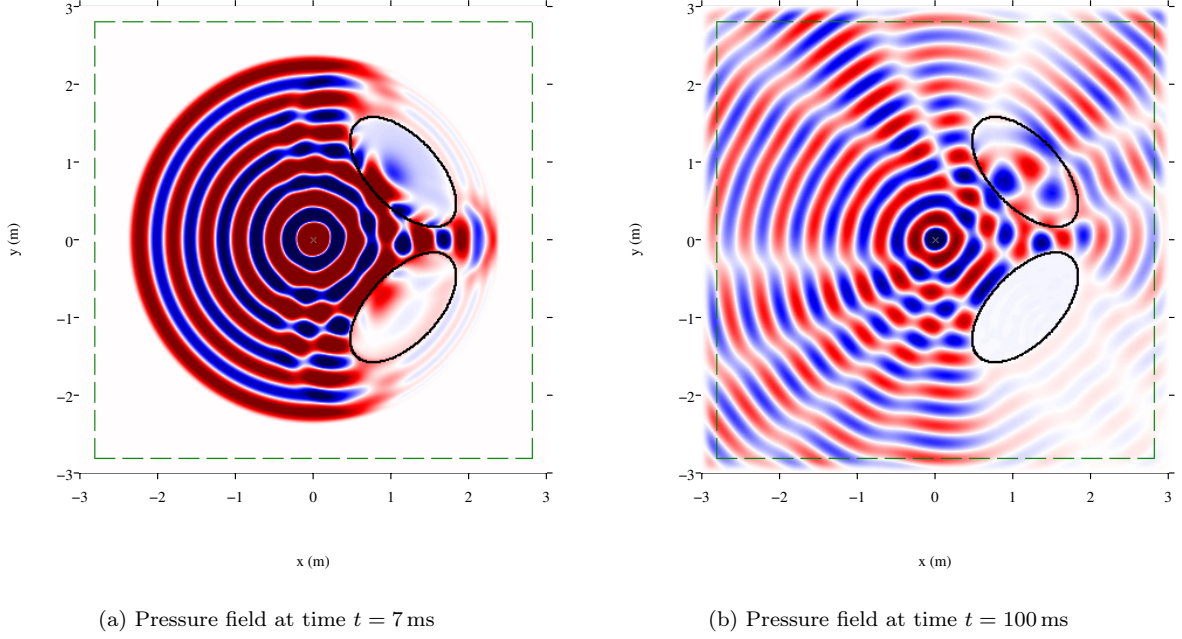


Figure 11: Snapshots of pressure field  $p$  in a 2D fluid medium with two scattering metamaterial obstacles. The excitation is time-harmonic at  $f_c = 800$  Hz.

Lastly, we consider the scattering of a plane-wave by an obstacle embedded in a fluid domain. In particular, our aim is to illustrate the different wave scattering phenomena associated with nonresonant and resonant scatterers respectively. To do so, the domain  $[-3, 3] \times [-3, 3] \text{ m}^2$  is discretized on a grid of  $600 \times 600$  points. An interface described by cubic splines is considered, emphasizing the ability of the immersed interface method to handle arbitrary-shaped geometries. The medium outside the interface is air ( $\rho = 1.3 \text{ kg m}^{-3}$ ,  $c_a = 340 \text{ m s}^{-1}$ ). The medium inside the interface is either a classical acoustic medium characterized by  $\rho = 2.6 \text{ kg m}^{-3}$ ,  $c_a = 500 \text{ m s}^{-1}$ , or the acoustic metamaterial considered in the previous examples. The computation is initialized by the right-going plane wave given by:

$$\begin{pmatrix} v_1 \\ v_2 \\ p \end{pmatrix} (x, y, t_0) = \begin{pmatrix} -1/c_a \\ 0 \\ \rho_a \end{pmatrix} G(t_0 - x/c_a),$$

where  $G$  is the time evolution of the source given in (28). The time shift is set to  $t_0 = -3$  ms to ensure that the incident plane wave does not intersect the interface at the initial time, see Figure 12. At each time step, periodic top-bottom boundary conditions are enforced. Figure 13 displays snapshots of the acoustic pressure at two instants. One observes in particular the complex pattern of the reflected wave in the resonant case, which is induced by the dispersive behavior of the metamaterial and the existence of backward propagating waves within the scatterer. These phenomena are analogous to these observed in the 1D configuration of Figure 8.

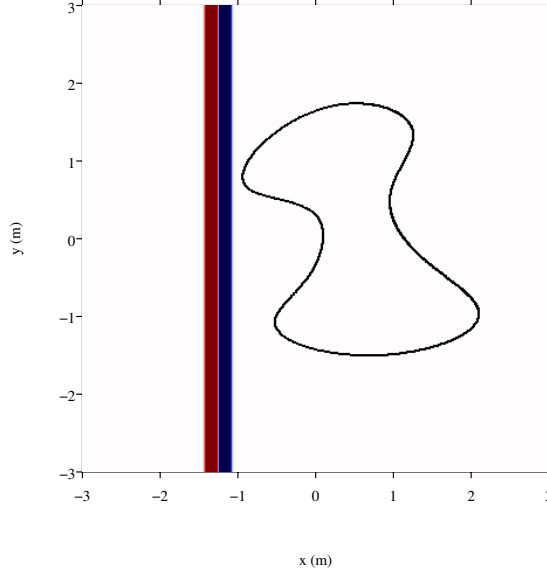


Figure 12: 2D simulation of scattering by an obstacle embedded in a fluid and illuminated by a plane wave. Snapshot of pressure field  $p$  at the initial time.

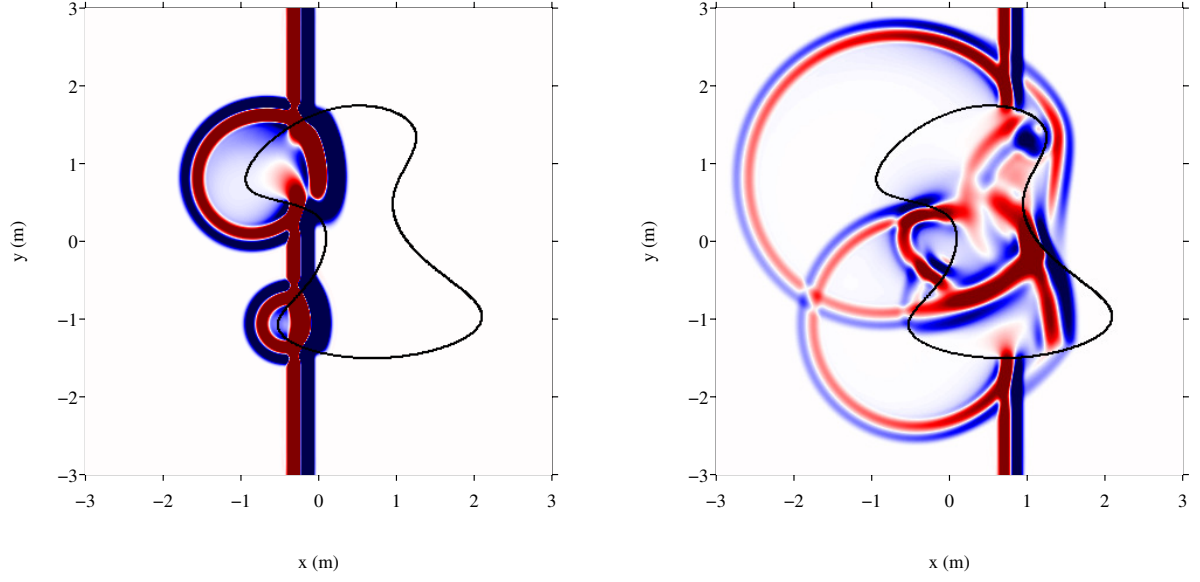
## 6. Conclusion

We have considered acoustic metamaterials that are characterized by frequency-dependent constitutive parameters. A time-domain formulation of the associated evolution equations is derived using a set of auxiliary fields and the properties of the resulting augmented system and of its solution have been analyzed. The numerical approach then proposed ensures both computational efficiency (Cartesian grid, optimal CFL stability condition) and high accuracy (high-order scheme, immersed interface method for interface problems). An effort has been made to validate the algorithms in comparison with semianalytical solutions. These methods have been implemented and made available online in the software PROSPERO (<http://prospero-software.science/>). With these numerical tools at hand, the broad spectrum of wave phenomena characteristic of acoustic metamaterials can be investigated in the time-domain. This allows in particular the study of interface problems as well as of wave propagation in double-negative materials which leads to perfect lenses [26]. These tools also allow to investigate transient scattering problems involving metamaterials, which have interesting applications in inverse problems and imaging.

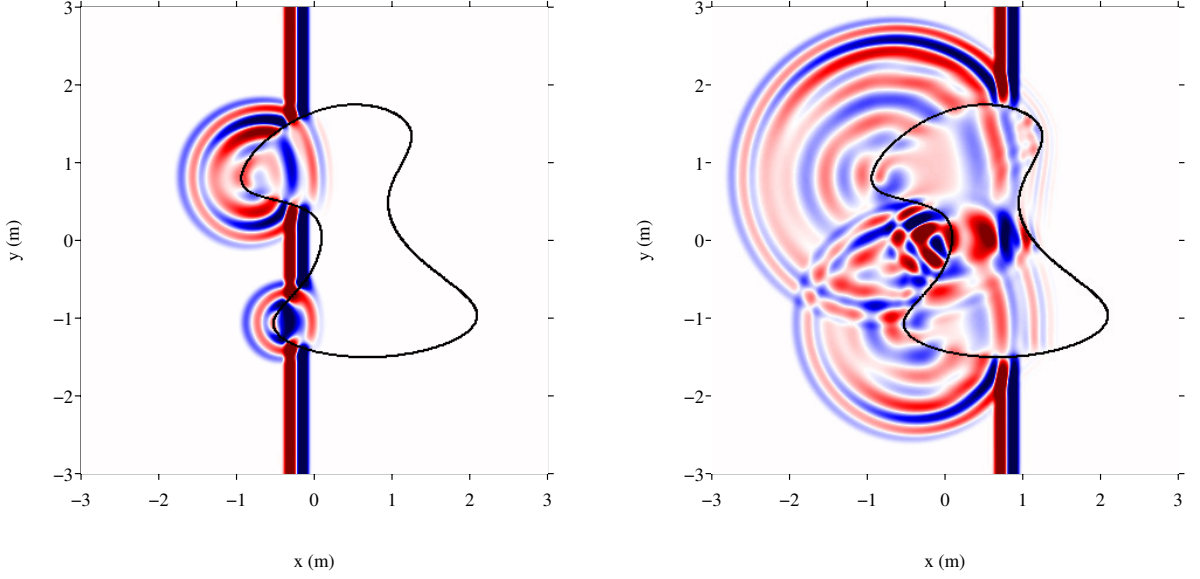
From a theoretical standpoint, there is a need for an in-depth mathematical analysis of the limiting absorption principle in the context of acoustic metamaterial. In particular, some insights could be gained by assessing quantitatively the equivalence between the frequency and time-domain problems and the properties of their solutions. Note that in the case of Maxwell's equations, the limiting absorption principle has been studied mathematically in [5] for interface problems involving a dispersive electromagnetic material.

The present study is based on a set of prototypical frequency-dependent constitutive parameters which are handled numerically in an efficient and accurate manner. Noticeably, the mathematical derivation of the effective properties of such metamaterials is not the focus of this paper. Future work directions include the time-domain simulations of alternative models, in particular those arising from the homogenization of locally resonant mechanisms [3, 39].

Lastly, among emerging applications of metamaterials, nonlinear behaviors are promising as they allow to design nonreciprocal or tunable materials [22, 20]. Extending our time-domain approach to nonlinear acoustic metamaterials would therefore be a fruitful contribution to this research effort. Preliminary works have been done on that subject: the propagation of nonlinear acoustic waves in a tube coupled with Helmholtz



(a) Acoustic scattering obstacle.



(b) Metamaterial scattering obstacle.

Figure 13: 2D simulation of scattering by an obstacle embedded in a fluid and illuminated by a plane wave. Snapshot of pressure field  $p$  at times  $t = 3$  ms and  $t = 6$  ms.



resonators has been addressed theoretically in [31, 34] and experimentally in [40], by considering one-way propagation. Considering two-way propagation will pave the way to the simulation of wave phenomena in nonlinear acoustic metamaterials.

*Acknowledgments.* The authors are thankful to Agnès Maurel, Kim Pham, Hajer Methenni and Maxence Cassier for insightful discussions.

*Funding.* The Authors have received funding from Excellence Initiative of Aix-Marseille University - A\*MIDEX, a French “Investissements d’Avenir” program in the framework of the Labex MEC.

- [1] Auriault J.L., Boutin C. 2012 Long wavelength inner-resonance cut-off frequencies in elastic composite materials. *Int. J. Sol. Struct.* **49**, 3269–3281.
- [2] Blanc E. 2013 *Time-domain numerical modeling of poroelastic waves: the Biot-JKD model with fractional derivatives*. PhD Thesis Aix-Marseille Université. (<https://tel.archives-ouvertes.fr/tel-00954506/>)
- [3] Bouchitté G, Schweitzer B. 2010 Homogenization of Maxwell’s equations in a split ring geometry. *Multiscale modeling & Simulation* **8**-3, 717–750.
- [4] Carcione J, Cavallini F. 1995 On the acoustic-electromagnetic analogy. *Wave Motion* **21**-2, 149–162.
- [5] Cassier M. 2014 *Etude de deux problèmes de propagation d’ondes transitoires: 1) Focalisation spatio-temporelle en acoustique; 2) Transmission entre un diélectrique et un métamatériau*. PhD Thesis, Ecole Polytechnique X. (<https://pastel.archives-ouvertes.fr/pastel-01023289>)
- [6] Cassier M., Joly P., Kachanovska M. 2017 Mathematical models for dispersive electromagnetic waves: An overview. *Computers & Mathematics with Applications* **74**-11, 2792–2830.
- [7] Cassier M, Hazard C, Joly P. 2017 Spectral theory for Maxwell’s equations at the interface of a metamaterial. Part I: Generalized Fourier transform. *Communications in Partial Differential Equations* **42**-11, 1707–1748.
- [8] Chaigne A, Kergomard J. 2016 *Acoustics of Musical Instruments*. Springer
- [9] Cheng Y, Xu JY, Liu XJ. 2008 One-dimensional structured ultrasonic metamaterials with simultaneously negative dynamic density and modulus. *Phys. Rev. B* **77**, 045134.
- [10] Craster RV, Guenneau S. 2013 *Acoustic Metamaterials: Negative Refraction, Imaging, Lensing and Cloaking*. Springer Series in Materials Science.
- [11] Deymier P. 2013 *Acoustic Metamaterials and Phononic Crystals*. Springer Series in Solid-State Science.
- [12] Ding Y, Liu Z, Qiu C, Shi J. 2007 Metamaterial with simultaneously negative bulk modulus and mass density. *Phys. Rev. Lett.* **99**, 093904.
- [13] Evans LC. 2010 *Partial differential equations*. Graduate Studies in Mathematics, American Mathematical Society.
- [14] Fang N, Xi D, Xu J, Ambati M, Srituravanich W, Sun C, Zhang X. 2006 Ultrasonic metamaterials with negative modulus. *Nature Materials* **5**, 452–456.
- [15] Felbacq D, Bouchitté G. 2005 Theory of mesoscopic magnetism in photonic crystals. *Phys. Rev. Lett.* **94**, 183902.
- [16] Flannery BP, Press WH, Teukolsky SA, Vetterling WT. 1992 *Numerical Recipes in C: the Art of Scientific Computing*. Second Edition, Cambridge University Press.
- [17] Friedrichs KO. 1958 Symmetric positive linear differential equations. *Comm. Pure Appl. Math.* **1**-1, 333–418.
- [18] Gralak B, Tip A. 2010 Macroscopic Maxwell’s equations and negative index materials. *J. Math. Phys.* **51**-5, 052902.
- [19] Gralak B, Maystre D. 2012, Negative index materials and time-harmonic electromagnetic field. *Comptes Rendus Physique* **13**-8, 786–799.
- [20] Haberman MR, Norris AN. 2016 Acoustic metamaterials. *Acoustics Today* **12**-3, 31–39.
- [21] Jimenez N, Romero-Garcia V, Pagneux V, Groby JP. 2017 Quasiperfect absorption by subwavelength acoustic panels in transmission using accumulation of resonances due to slow sound. *Phys. Rev. B* **95**, 014205.
- [22] Khajehtourian R, Hussein MI. 2014 Dispersion characteristics of a nonlinear elastic metamaterial. *AIP Advances* **4**, 124308.
- [23] Lee SH, Park CM, Seo YM, Wang ZG, Kim CK. 2009 Acoustic metamaterial with negative density. *Phys. Lett. A* **373**, 4464–4469.
- [24] Lee SH, Wright OB. 2016 Origin of negative density and modulus in acoustic metamaterials. *Phys. Rev. B* **93**, 024302.
- [25] LeVeque R.J. 2002 *Finite Volume Methods for Hyperbolic Problems*. Cambridge University Press.
- [26] Li J, Chan CT. 2004 Double-negative acoustic metamaterial. *Phys. Rev. E* **70**, 055602.
- [27] Li J, Wood A. 2007 Finite element analysis for wave propagation in double negative metamaterials. *J. Scient. Comput.* **32**-2, 263–286.
- [28] Li J, Huang Y. 2013 *Time-Domain Finite Element Methods for Maxwell’s Equations in Metamaterials*. Springer.
- [29] Liu Z, Zhang Z, Mao Y, Zhu YY, Yiang Z, Chan CT, Sheng P. 2000 Locally resonant sonic materials. *Science* **289**, 1734–1736.
- [30] Lombard B. 2010 *Modélisation numérique de la propagation et de la diffraction d’ondes mécaniques*. Habilitation Thesis Aix-Marseille Université. (<https://tel.archives-ouvertes.fr/tel-00448897/>)
- [31] Lombard B, Mercier JF. 2014 Numerical modeling of nonlinear acoustic waves in a tube with Helmholtz resonators. *J. Comput. Phys.* **259**, 421–443.
- [32] Lombard B, Maurel A, Marigo JJ. 2017 Numerical modeling of the acoustic wave propagation across a homogenized rigid microstructure in the time domain. *J. Comput. Phys.* **335**, 558–577.
- [33] Ma G, Sheng P. 2016 Acoustic metamaterials: from local resonances to broad horizons. *Sci. Adv.* **2**, 501595.

- [34] Mercier JF, Lombard B. 2017 A two-way model for nonlinear acoustic waves in a nonuniform lattice of Helmholtz resonators. *Wave Motion* **72**, 260–275.
- [35] Milton GW, Willis JR. 2007 On modifications of Newton’s second law and linear continuum elastodynamics. *Proc. R. Soc. A* **463**, 855–880.
- [36] Moler CB, Van Loan CF. 2003 Nineteen dubious ways to compute the exponential of a matrix, twenty-five years later. *SIAM Review* **45**, 3–49.
- [37] Nguyen H-M, Violes V. 2018 Electromagnetic wave propagation in media consisting of dispersive metamaterials. *Comptes Rendus Mathématique* **356**, 757–775.
- [38] Pendry JB. 2000 Negative refraction makes a perfect lens. *Phys. Rev. Lett.* **85**, 3966.
- [39] Pham K, Maurel A, Marigo JJ. 2017 Two scale homogenization of a row of locally resonant inclusions: the case of anti-plane shear waves. *J. Mech. Phys. Sol.* **106**, 80–94.
- [40] Richoux O, Lombard B, Mercier JF. 2015 Generation of acoustic solitary waves in a lattice of Helmholtz resonators. *Wave Motion* **56**, 85–99.
- [41] Romero-Garcia V, Krynkin A, Garcia-Raffi LM, Umnova O, Sanchez-Perez JV. 2013 Multi-resonant scatterers in sonic crystals: Locally multi-resonant acoustic metamaterial. *J. Sound Vib.* **332**, 184–198.
- [42] Sanchez-Palencia, E. 2013 *Non-Homogeneous Media and Vibration Theory*. Springer, Berlin, Heidelberg.
- [43] Schwartzkopff T, Dumbser M, Munz C. 2004 Fast high-order ADER schemes for linear hyperbolic equations. *J. Comput. Phys.* **197**-2, 532–539.
- [44] Seo YM, Park JJ, Lee SH, Park CM, Kim CK, Lee SH. 2012 Acoustic metamaterial exhibiting four different sign combinations of density and modulus. *J. Appl. Phys.* **111**, 023504.
- [45] Tip A. 1998 Linear absorptive dielectrics. *Phys. Rev. A* **57**-6, 4818.
- [46] Violes V. 2016 *Problèmes d’interface en présence de métamatériaux : modélisation, analyse et simulations*. PhD Thesis Université Paris Saclay. (<https://pastel.archives-ouvertes.fr/tel-01426226>)
- [47] Yang Z, Mei J, Yang M, Chan NH, Sheng P. 2008 Membrane-type acoustic metamaterial with negative dynamic mass. *Phys. Rev. Lett.* **101**, 204301.

## Appendix A. Proofs of some results of Section 3

### Appendix A.1. Proof of Property 4

To analyze the energy of the augmented system, one considers an arbitrary bounded domain  $\mathcal{D} \subset \mathbb{R}^d$ . From (7), it follows

$$\int_{\mathcal{D}} \left\{ \mathbf{U}^\top \mathbf{E} \frac{\partial}{\partial t} \mathbf{U} + \sum_{j=1}^d \mathbf{U}^\top \mathbf{E} \mathbf{A}_j \frac{\partial}{\partial x_j} \mathbf{U} \right\} d\mathbf{x} = \int_{\mathcal{D}} \left\{ \mathbf{U}^\top \mathbf{E} \mathbf{S} \mathbf{U} + \mathbf{U}^\top \mathbf{E} \mathbf{F} \right\} d\mathbf{x}. \quad (\text{A.1})$$

Exploiting the symmetry property 3 of the featured matrices, one has

$$\mathbf{U}^\top \mathbf{E} \frac{\partial}{\partial t} \mathbf{U} = \frac{1}{2} \frac{\partial}{\partial t} (\mathbf{U}^\top \mathbf{E} \mathbf{U}) \quad \text{and} \quad \mathbf{U}^\top \mathbf{E} \mathbf{S} \mathbf{U} = -\frac{\gamma \Omega_\kappa^2}{\kappa_a} |[\mathbf{U}]_{m-1}|^2,$$

since  $\tilde{\mathbf{S}}$  being skew-symmetric it satisfies  $\mathbf{U}^\top \tilde{\mathbf{S}} \mathbf{U} = \mathbf{0}$ . Moreover, integrating by part the second term in (A.1) for all  $j = 1, \dots, d$ , yields the following identity by symmetry

$$\int_{\mathcal{D}} \mathbf{U}^\top \mathbf{E} \mathbf{A}_j \frac{\partial}{\partial x_j} \mathbf{U} d\mathbf{x} = \frac{1}{2} \int_{\partial \mathcal{D}} \mathbf{U}^\top \mathbf{E} \mathbf{A}_j n_j \mathbf{U} ds,$$

where  $n_j$  denotes the  $j$ -th component of the unit outward normal  $\mathbf{n}$  on the domain boundary  $\partial \mathcal{D}$ . Inserting the previous identities in (A.1) entails

$$\frac{1}{2} \frac{d}{dt} \int_{\mathcal{D}} \mathbf{U}^\top \mathbf{E} \mathbf{U} d\mathbf{x} + \frac{1}{2} \int_{\partial \mathcal{D}} \mathbf{U}^\top \mathbf{E} \mathbf{A}(\mathbf{n}) \mathbf{U} ds = - \int_{\mathcal{D}} \frac{\gamma \Omega_\kappa^2}{\kappa_a} |[\mathbf{U}]_{m-1}|^2 d\mathbf{x} + \int_{\mathcal{D}} \mathbf{U}^\top \mathbf{E} \mathbf{F} d\mathbf{x}, \quad (\text{A.2})$$

where  $\mathbf{A}(\mathbf{n})$  is defined as in (10). In the case of an unbounded domain, the integral along  $\partial \mathcal{D}$  vanishes when  $\mathbf{U} \in L^2(\mathbb{R}^d)^m$ . Finally, using the definitions (5), (6) and (12), then the above identity yields Property 4.



*Appendix A.2. Proof of Theorem 3.1*

Using the positive-definite diagonal matrix  $\mathbf{E}$  to symmetrize the augmented system (7) one obtains

$$\begin{cases} \mathbf{E} \frac{\partial}{\partial t} \mathbf{U} + \sum_{j=1}^d \mathbf{E} \mathbf{A}_j \frac{\partial}{\partial x_j} \mathbf{U} = \mathbf{E} \mathbf{S} \mathbf{U} + \mathbf{E} \mathbf{F}, & (t > 0) \\ \mathbf{U}(\mathbf{x}, 0) = \mathbf{U}_0. \end{cases} \quad (\text{A.3})$$

The matrix  $\mathbf{E} \mathbf{A}$  being diagonalizable with real eigenvalues (by properties 1 and 3) then, by definition, this system is hyperbolic. Yet, as all eigenvalues are not distinct, it is not strictly hyperbolic. Friedrichs' theory on symmetric hyperbolic systems, see [17] and [13], applied to (A.3) yields the sought existence and regularity results.

*Appendix A.3. Proof of Property 5*

To prove the stability property 5 one must show that the angular frequencies in (16) satisfy  $\Im m(\omega) \geq 0$  and that the nondissipative property  $\gamma = 0$  entails  $\Im m(\omega) = 0$ . Considering an eigenpair  $(\omega, \mathbf{v}) \in \mathbb{C} \times \mathbb{C}^m$  of the matrix  $\mathbf{A}'(\mathbf{k})$ , then one has by definition

$$\mathbf{A}(\mathbf{k})\mathbf{v} - i\mathbf{S}\mathbf{v} = \omega \mathbf{v}. \quad (\text{A.4})$$

Now, using  $\mathbf{E}$  to symmetrize (A.4) and pre-multiplying by  $\mathbf{v}^\dagger = \bar{\mathbf{v}}^\top$  entails

$$\mathbf{v}^\dagger \mathbf{E} \mathbf{A}(\mathbf{k}) \mathbf{v} - i \mathbf{v}^\dagger \mathbf{E} \mathbf{S} \mathbf{v} = \omega \mathbf{v}^\dagger \mathbf{E} \mathbf{v}, \quad (\text{A.5})$$

where one can assume without loss of generality that  $\mathbf{v}$  satisfies  $\mathbf{v}^\dagger \mathbf{E} \mathbf{v} = 1$ . Owing to Property 3, the matrices  $\mathbf{E} \mathbf{A}(\mathbf{k})$  and  $\tilde{\mathbf{S}}$  can be diagonalized so that there exist some matrices  $\mathbf{D}, \mathbf{P} \in \mathcal{M}_m(\mathbb{R})$ , that depend on  $\mathbf{k}$ , and  $\mathbf{\Sigma}, \mathbf{U} \in \mathcal{M}_m(\mathbb{C})$  with  $\mathbf{D}$  and  $\mathbf{\Sigma}$  being diagonal,  $\mathbf{P}$  orthogonal and  $\mathbf{U}$  unitary such that

$$\mathbf{E} \mathbf{A}(\mathbf{k}) = \mathbf{P} \mathbf{D} \mathbf{P}^\top \quad \text{and} \quad \mathbf{E} \mathbf{S} = \mathbf{U} \mathbf{\Sigma} \mathbf{U}^\dagger - \frac{\gamma \Omega_\kappa^2}{\kappa_a} \tilde{\mathbf{I}}_{m-1}.$$

Inserting this in (A.5) yields

$$(\mathbf{P}^\top \mathbf{v})^\dagger \mathbf{D} (\mathbf{P}^\top \mathbf{v}) - i (\mathbf{U}^\dagger \mathbf{v})^\dagger \mathbf{\Sigma} (\mathbf{U}^\dagger \mathbf{v}) + i \frac{\gamma \Omega_\kappa^2}{\kappa_a} \mathbf{v}^\dagger \tilde{\mathbf{I}}_{m-1} \mathbf{v} = \omega.$$

For all nonzero  $\mathbf{v} \in \mathbb{C}^n$  one has  $(\mathbf{P}^\top \mathbf{v})^\dagger \mathbf{D} (\mathbf{P}^\top \mathbf{v}) \in \mathbb{R}$  while  $(\mathbf{U}^\dagger \mathbf{v})^\dagger \mathbf{\Sigma} (\mathbf{U}^\dagger \mathbf{v})$  is a purely imaginary number since the diagonal matrix  $\mathbf{\Sigma}$  contains the eigenvalues of the skew-symmetric matrix  $\tilde{\mathbf{S}}$  that are either zero or pairs of purely imaginary complex conjugates. Therefore, the previous equation entails

$$\Im m(\omega) = \frac{\gamma \Omega_\kappa^2}{\kappa_a} |[\mathbf{v}]_{m-1}|^2, \quad (\text{A.6})$$

which concludes the proof of Property 5.

Note that, as the entry  $m - 1$  of an eigenvector  $\mathbf{v}$  corresponds to the auxiliary field  $q$ , the above proof is fully consistent with the energy property (13): any eigenvector such that  $q = 0$  corresponds to a nonattenuated propagating mode with  $\Im m(\omega) = 0$ . Conversely, as soon as  $q \neq 0$  then the corresponding mode is attenuated exponentially in time according to (A.6) when  $\gamma \neq 0$ .